Correlation of Subregional Hippocampal Thickness Abnormalities with Positron Emission Tomography Phosphorylated Tau Measurements in Patients with Mild Cognitive Impairment and Alzheimer's Disease

by

Muhammad Mujtaba Siddique

A thesis submitted in partial fulfillment of the requirements for the degree of

Master of Science

Department of Medicine
University of Alberta

Abstract

Alzheimer's disease (AD) is the most common cause of dementia and is an emerging public health crisis with 150 million cases projected globally by 2050. Biomarkers are playing an emerging role in AD research - however, existing biomarkers have substantial limitations. Magnetic Resonance Imaging (MRI) holds advantages over existing biomarkers as it is non-invasive and does not involve exposure to ionizing radiation. This project aims to utilize MR images to measure subfield thickness throughout the hippocampal long axis using HippUnfold, a recently released open-source automated hippocampal segmentation software, and to correlate these measurements with Positron Emission Tomography (PET) phosphorylated tau (pTau), an extensively validated imaging biomarker for AD.

High resolution (0.39x0.39x2mm) Hippocampal MR Images acquired by the Alzheimer's Disease Neuroimaging Initiative (ADNI) were used in the analysis. The right hemisphere cohort included control, n= 281, mild cognitive impairment (MCI, n =219), and AD, (n = 44) and the left hemisphere cohort included control, n= 278, mild cognitive impairment (MCI, n =205), and AD, (n = 41). HippUnfold provided automated segmentation and computed thickness measurements for 5 hippocampal subfields: subiculum and cornu ammonis (CA) 1-4 throughout the entire hippocampal long axis. Previously acquired PET measurements for phosphorylated tau were downloaded from the ADNI database and correlated with thickness measurements along the hippocampal long axis using linear regression models.

In our analyses - thickness measurements were strongly correlated with the degree of tau deposition quantified with tau PET. Specifically, we found significant cluster correlation ($p < 0.05$) throughout the long axis when comparing reduced hippocampal subfield thickness to PET phosphorylated tau Standard Uptake Volume Ratios (SUVRs). Furthermore, we identified

regional specificity of maximal thickness abnormalities in our cohort in the body of the subiculum and CA1 in both hemispheres and the head region of CA2-4 in the right hemisphere. Our data add to the previous scientific literature demonstrating subfield-specific hippocampal volume loss throughout the hippocampus in patients with AD.

Preface

This thesis is the original work by Mujtaba Siddique. No part of this thesis has been previously published.

Acknowledgments

I would like to thank Dr. Trevor Steve and Dr. Richard Camicioli for their supervision, guidance, and support as my supervisors for this project. I would like to thank Dr. Tejas Sankar for his feedback on my project as a committee member and with providing me with guidance as well. I would like to thank Dr. Alan Wilman for his feedback and insights on my thesis. I would like to thank Luiciana for helping me get started with using HippUnfold. Finally, I would like to thank Mohamed Yousef for all of his work with helping me use and understand HippUnfold, Python, and BrainStat. I would finally like to thank S.D, I.V, D.M, J.R, M.S, S.A, and my parents for their support during this time.

Table of Contents

List of Tables

List of Figures

Chapter 1. Introduction

1.1 Alzheimer's Disease

Dementia is a common, disabling, disease that places a huge burden on careers, families, and medical services. Alzheimer's disease (AD) is the most common cause of dementia, and the prevalence of dementia is predicted to increase over time associated with the aging of the population [1,2]. AD also has a substantial annual economic burden, costing an estimated 1313.4 billion worldwide which is predicted to climb as the population continues to age [3]. AD is a devastating neurodegenerative disorder that affects millions of individuals around the world with the estimated global number of patients surpassing 50 million, which will impact not only many patients but also the millions of family members, friends, and health care professionals who help in caring for them [4].

The symptoms of the disease can vary for each individual, but the first clinical and most prominent manifestation of AD is selective memory impairment [5]. This includes impairment of declarative episodic memory, which are memories of previous life events (especially memory of recent events) [6]. This type of memory is served by structures of the medial temporal lobe (MTL) such as the hippocampus, entorhinal cortex, perirhinal cortex, and parahippocampal cortex which are essential for normal memory function [7]. Semantic memory, which includes our knowledge about facts, concepts, and ideas is impaired later in the disease course [8]. Diagnosis of memory impairment is done through recall tests where objects are learned and are recalled later. Additional symptoms experienced by patients with AD include impairment in executive functioning, impairment in judgment/problem-solving, compromised multitasking, confusion with respect to place and time, difficulties completing familiar tasks, loss of insight into deficits, and language impairment [9,10]. Symptoms such as apraxia, seizures, sleep disturbances, and motor signs are less common [11]. A minority of patients with AD do not present in the classic fashion of progressive amnestic dementia. Atypical presentations of AD can occur and involve non-amnestic and early-onset forms of the disease such as posterior cortical atrophy (PCA), which is characterized by visual impairments, and logopenic variant primary progressive aphasia (lvPPA), in which patients have difficulties finding words causing hesitant speech [11]. LvPPA is a clinical subtype of primary progressive aphasia (PPA) which is typically related to AD

neuropathology, whereas other variants of PPA such as nonfluent progressive aphasia are usually due to non-AD tauopathies [12,13].

The average life expectancy after diagnosis can range from 4.2 years to 10 years depending on the severity of the condition and the age of the individual at onset [14,15]. Validated cognitive tests such as the Mini-Mental State Examination (MMSE) and the Montreal Cognitive Assessment (MoCA) are used to measure cognitive deficits and the progress of the disease over time[16]. AD is diagnosed clinically based on the history of symptom onset, progressive course of cognitive decline, documentation of cognitive impairments along with testing for other cognitive domains including visual-spatial skills, attention, concentration abilities, and executive functioning [17]. The diagnostic criteria for probable and possible AD dementia are established by both the National Institute on Aging and the Alzheimer's Association (NIA-AA) and the Diagnostic and Statistical Manual of Mental Disorders (DSM) criteria for AD [18]. The degree of functional impairment associated with cognitive decline is used to differentiate between mild cognitive impairment (MCI) and AD. MCI is defined as objective cognitive dysfunction (typically with early involvement of recent memory) with preserved adaptive functioning with respect to activities of daily living – and is considered an early stage of AD [19]. The conversion rate from MCI to AD is approximately 10-15% per year and approximately 80% of patients with MCI have progressed to AD at 6-year follow-up [20,21]. Patients with MCI are therefore at the earliest stages of the disease continuum when therapeutic intervention is most likely to be beneficial – and are thus important in any investigation related to diagnosis, prognosis, and treatment of AD.

Definitive diagnosis of AD is based on compatible clinical presentation with characteristic neuropathological findings found post-mortem. Gross autopsy typically demonstrates cerebral cortical atrophy with prominent atrophy of the hippocampus [22], whereas histological examination is required to demonstrate the two characteristic neuropathological changes associated with AD. The first major neuropathological change consists of senile plaques, which are associated with the accumulation of the beta-amyloid (Aβ) peptide in the brain [23]. The Aβ (4 kDa) peptide is derived from a larger amyloid precursor protein (APP), which is a highly conserved transmembrane glycoprotein [24]. Aβ peptides, which are formed via the action of secretases, are released from the plasma membrane and may accumulate in the brain

[24,25]. Proteolytic cleavage of APP by β-secretase and γ-secretases generates insoluble Aβ, whereas cleavage by α-secretase results in the release of non-amyloidogenic, soluble, APPα [24,25,26]. The APP gene is located on chromosome 21 and encodes the protein APP. Mutations in this gene are associated with 10-15% of early-onset AD cases. Mutations in this gene result in increased production of Aβ42, and an increased ratio of Aβ42 to Aβ40 [25]. Aβ42 is longer and more prone to fibril formation (with associated neurotoxicity) in comparison to Aβ40 and is therefore postulated to play an important role in the pathogenesis of AD [27]. Aβ oligomers interact with neurons and cause the activation of inflammatory cascades and oxidative stress, which leads to neuronal death [27]. Additional genes involved in AD pathogenesis are presenilin-1 (PSEN1) and presenilin-2 (PSEN2), which are located on chromosome 14 and 1 respectively. In particular, PSEN 1 mutations can be identified in up to 50% of patients with early-onset AD [28]. PSEN 1 plays a role in calcium signaling and membrane trafficking and is one component of the complex responsible for γ-secretase cleavage of APP to release Aβ peptides of varying lengths [29]. Mutations in PSEN 1 increase the generation of the highly fibrillogenic Aβ42 species and enhance the accumulation of Aβ in the brain. Mutations in PSEN 2 may also alter the cleavage activity of γ-secretase and increase the ratio of Aβ42 to Aβ40 with resultant accumulation of Aβ due to reduced Aβ clearance in the brain [29].

The second neuropathological hallmark of AD is neurofibrillary tangles (NFT) which are abnormal fibrous inclusions throughout the brain [30]. The primary constituent of these tangles is abnormally phosphorylated tau protein, as hyper-phosphorylation of tau causes the formation of tau aggregates as neurofibrillary tangles [31]. Fluorescent dyes and immunohistochemical approaches use antibodies that are directed against abnormally phosphorylated Tau. Tau pathology spreads in a stereotyped manner with initial involvement of the entorhinal cortex and hippocampus, with subsequent spread to adjacent neocortical mesial temporal structures including the inferior temporal region [32,33]. Critically, the extent of neurofibrillary tangle depositions in AD correlates with the degree of neuronal loss and severity of dementia symptoms [34].

1.2 Biomarkers in Alzheimer's Disease

1.2.1 Clinical Assessment Limitations

AD is diagnosed clinically based on a characteristic history with associated cognitive deficits measured with cognitive tests such as the MMSE or MoCA [35]. However, previous studies have demonstrated that clinical diagnostic accuracy for the diagnosis of AD is 77% [36]. There are several potential reasons for this finding. Firstly, during clinical assessments a patient can present clinically as cognitively unimpaired yet at autopsy may demonstrate neuropathological changes consistent with AD. For example, one previous study found that 60% of cognitively unimpaired patients over the age of 80 years had AD neuropathological changes at autopsy [37]. A second reason why clinical diagnoses are insufficient for definitive diagnosis of AD is that the cogntive symptoms assessed by these scales may be caused by a wide range of neuropathological entities such as frontotemporal dementias [38,39], dementia with Lewy bodies (DLB), Parkinson's disease dementia (PDD), and cerebrovascular disease [39].

In summary, since its initial description AD has been diagnosed based on typical clinical symptoms. However, given that the clinical diagnosis of AD has an imperfect correlation with pathology – new methods of differentiating the pathological causes of dementia in vivo have recently been developed, such as analyzing biomarkers [40]. These methods are intended to overcome the limited sensitivity and specificity of AD clinical diagnosis – by assisting in differentiating different neuropathological diseases from one another [41]. These efforts are relevant to the evaluation of disease-modifying agents for AD, by enabling subject enrichment in clinical trials.

1.2.2 What are Biomarkers.

Biomarkers are characteristics that can be measured objectively and are analyzed as indicators of normal biological processes and/or pathogenic processes. The world health organization (WHO) defines biomarkers as a substance or process that is measured in the body, or its products which can aid in predicting the outcome of the disease [42]. Biomarkers are chosen if they show strong associations with specific clinical conditions and outcomes of the disease they are trying to assess[43]. Biomarkers can improve our understanding of disease pathogenesis which can translate into new approaches for certain diagnoses and treatments. In support of the relevance of biomarkers to drug development, previous studies have shown that up to three-quarters of the

drugs in clinical use have used biomarkers in their clinical trials [44]. Clinical endpoints are defined as variables that defines an individual's well-being and health [42]. It is important to note that some biomarkers may not correlate with clinical symptoms, or the patient's well-being, highlighting the importance of establishing a relationship between candidate biomarkers and clinical outcomes [43]. This is important when selecting biomarkers for clinical trials - as clinical endpoints are the primary goal of clinical research to demonstrate efficacy and result in the approval of any therapeutic intervention in clinical practice.

The need for biomarkers is particularly relevant to AD research because clinical endpoints are problematic in clinical trials of disease-modifying agents for AD. For example, the clinical endpoints of worsening memory, declining adaptive function, and death occur over a protracted time course in AD and therefore are suboptimal outcome measures for AD clinical trials [42]. Biomarkers can therefore play a critical role as surrogate endpoints to substitute for clinical endpoints. However, biomarkers must be accompanied by scientific evidence suggesting there is a relationship between the biomarker and its ability to predict clinical outcomes (e,g. cognitive function) [44]. Since beta-amyloid plaques , neurofibrillary tau deposits, and neuronal loss are the key neuropathological features of AD, existing biomarkers for AD target these aspects of the disease pathophysiology [37].

1.2.3 Positron Emission Tomography Biomarkers

Positron Emission Tomography (PET) imaging uses tracers that contain positron-emitting radioisotopes, which are injected intravenously [45]. The distribution and magnitude of radio-isotope accumulation are then measured, providing insight into the location and distribution of the molecule of interest in the brain [45]. Aβ- and tau-specific PET ligands have been developed and validated in patients with AD [46]. The detection of amyloid pathology has been described using multiple tracers including [18F]F-Florbetapir, 18F-flutemetamol, and 18F-florbetaben [47]. Most recently - [18F]Flortaucipir (also known as tau PET) has been extensively studied to measure phosphorylated tau (pTau) deposits and monitors the characteristic pattern of NFT accumulation in AD patients[48].

1.2.4 Comparing Different Biomarkers Specific to Alzheimer's Disease

Recent studies have proposed the ATN system for AD diagnosis - where both Aβ (A) and tau deposits (T) are required to fulfill the criteria for AD, whereas measures of neuronal injury (N) are used to determine the disease severity. An example of the ATN profiling system is that patients without neuronal injury (A+T+N-) and with neuronal injury (A+T+N+) are both classified as AD, whereas those with neuronal injury are at the more severe end of the Alzheimer's continuum [49]. A key future direction in research is to increase the widespread use of amyloid, tau, and neuronal injury biomarkers in patients with AD by exploring biomarkers that are more widely available, less invasive, and less expensive. [37,50]. Previous studies have compared imaging biomarkers with fluid biomarkers to determine which have better predictive values for clinical manifestations such as cognitive decline. In addition, a key aspect of neuroimaging biomarker development is comparison to established and validated AD biomarkers for amyloid, tau, and neuronal injury.

Initial work by Ossenkoppele et al. in 2018 suggested that PET Tau positivity was a better predictor of short-term cognitive decline than PET Aβ or cerebral spinal fluid (CSF) pTau in AD patients [51]. These authors found that the presence of pathological levels of abnormally phosphorylated tau in the brain when measured with PET tau imaging predicted a steeper decline in cognition longitudinally, irrespective of the CSF measurements. In addition, this study found that control patients had higher rates of CSF amyloid and tau positivity in comparison to tau PET positivity, suggesting that tau PET biomarkers have more specificity [51].

Bucci et al.[52] have subsequently performed a comprehensive evaluation of the performance of various AD biomarkers. These authors measured standard uptake volume ratios (SUVRs) for a tau PET biomarker, Flortaupir AV- 1451 comparing target (predicted to demonstrate abnormal deposition) and reference (control) regions [53,54] in order to quantify abnormal phosphorylated tau accumulation in patients with AD [55]. Specifically, SUVRs were measured from the inferior temporal cortex, entorhinal cortex, and a combined Meta Temporal Region (METAROI) which is comprised of the bilateral entorhinal, amygdala, fusiform, inferior and middle temporal cortices [51,56,57] whereas the inferior cerebellar region was used as the reference (control) region. They found that only the profiles that were PET tau positive,

irrespective of CSF tau status, (i.e either CSF+/PET+, CSF-/PET+) showed a significant decline in cognition and overall episodic memory (relative to CSF-/PET-). In this study, patients with amyloid and tau PET positivity (A+T+) had a significant decline in cognition while PET Aβ positivity alone (A+T-) did not predict the severity of cognitive decline [52]. Furthermore, CSF tau levels were less predictive of cognitive decline in comparison to tau PET [52]. These results demonstrate that tau PET positivity is a better predictor of cognitive decline in patients with AD, in comparison to PET Aβ or CSF pTau positivity [52], suggesting that tau PET is a powerful biomarker for AD [58].

1.2.6 Limitations

As discussed above, previous research has suggested that tau PET imaging can document pathological tau accumulation which is associated with longitudinal worsening of cognitive function [59]. However, while PET tau imaging has emerged as a powerful biomarker for AD it also has important limitations [60]. First, PET scanning involves exposure to ionizing radiation which is dependent on the level of radioactivity of the tracer injected, the half-life, and the number of injections [61]. This somewhat limits its use for monitoring disease progression over time where frequent scans over many years may be required. Second, tau PET radiotracers must be injected intravenously in patients, which can be uncomfortable for some patients and many are reluctant to have these procedures done [40]. Another key limitation of tau PET imaging relates to limited availability as the required radiotracers to perform tau PET are not widely available. Therefore, an active area of current AD research is to develop novel biomarkers which can overcome the key limitations of tau PET listed above.

1.3 MRI

1.3.1 MRI as a Biomarker

MRI is a non-invasive imaging modality that can detect changes in patients with AD and can also be used to monitor disease progression[62]. One of the brain regions that is most severely affected in AD is the hippocampus - as this is one of the first regions affected by AD pathology [63]. The hippocampus is a structure that is part of the limbic system, a system that plays a role in memory, emotional response, and behavior [64]. In particular, the hippocampus is integral to consolidating and retrieving declarative memory, which are memories for facts and events [64].

The hippocampus also participates in the transfer of memories from short-term memory into long-term memory, so damage to the hippocampus from any cause typically results in memory impairment and the inability to form new memories [65]. The earliest changes detected using structural MRI in patients with AD are in the medial temporal lobe structures, such as the entorhinal cortex, perirhinal cortex, and the hippocampus. Reduced hippocampal volume as well as atrophy of these adjacent mesial temporal cortices are associated with the severity of memory deficits in patients with AD [66,67].

1.3.2 Advantages and Limitations of MRI

MRI is a very promising modality for AD biomarker development as it is widely available, non-invasive, and does not involve exposure to ionizing radiation. However, MRI is currently considered a late biomarker for AD in comparison to tau and amyloid measurements. Jack et al. have found that beta-amyloid and phosphorylated tau PET biomarkers are "upstream" biomarkers meaning abnormalities on these measures occur earlier in patients with AD, whereas neurodegenerative biomarkers (such as structural MRI) are considered "downstream" or late biomarkers, highlighting the current limitation of conventional structural MRI as a biomarker for AD [68]. These limitations of current methods highlight the need for more sensitive MRI-based biomarkers which are correlated with existing (invasive) AD biomarkers.

1.3.3 Hippocampal Subfields and Anatomy

The hippocampus can be divided into three sections (head, body, and tail) ranging from most anterior to most posterior based on the macrostructural features of the hippocampus [69]. In addition, the hippocampus is made of several distinct subfields which are continuous throughout the longitudinal axis of the structure. As seen in Figure 1, the hippocampus can be divided into at least 6 subfields: Subiculum, Cornu Ammonis 1-4 (CA1-4), and the dentate gyrus (DG) [69]. The hippocampal body demonstrates a characteristic C-shaped configuration with the DG being in the most inward part of the folding, followed by CA4 all the way to CA1 – with the subiculum being located on the outermost aspect of the folding where it is adjacent to the medial temporal lobe neocortex (entorhinal cortex) [70]. The subiculum is involved in verbal delayed recall performance, while the dentate gyrus, CA1, and the CA4 regions are most strongly associated with delayed memory recall performance [71]. CA2, CA3, and the subiculum are involved during

learning, and the CA1 and posterior parts of the subiculum are involved during the retrieval of novel associations[71].

Figure 1.

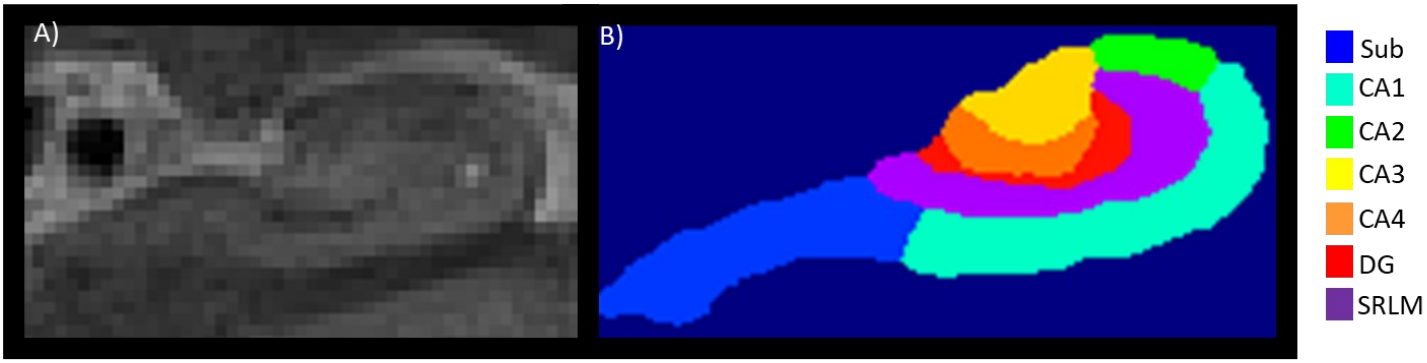

Figure 1. In Vivo Hippocampal Subfield volumetry with HippUnfold

A) Coronal T2 Weighted MR Image (resolution - 0.39 mm x 0.39 mm x 2.0 mm) of the hippocampal body
B) HippUnfold-based delineation of hippocampal subfields: Sub= Subiculum, CA = Cornu Ammonis, DG = Dentate gyrus, and SRLM=stratum radiatum, Lacunosum, and moleculare.

1.3.4 Whole Hippocampus and Subfield Volumes

MRI studies have been performed on the hippocampus to detect atrophy patterns in patients with AD. Studies have achieved this by using the volume from segmentations, voxel-based morphometry approaches, and surface mesh modeling approaches. Studies have found that compared to CN and MCI individuals, AD individuals have significantly reduced subiculum and CA1 volumes [72,73]. These studies have also found reduced subiculum volumes in MCI individuals who convert from MCI to AD when compared to MCI individuals who did not convert, suggesting that hippocampal subfield atrophy can be a predictor of conversion from MCI to AD [73]. In addition, previous studies have demonstrated that the CA2 region is relatively spared in volumetric analysis of the hippocampus when comparing between CN, MCI, and AD [74].

In the literature, it is known that the pattern of atrophy is consistent with the pattern of neurofibrillary tangles progression in the course of AD. Different regions of the hippocampus are known to be affected differentially by NFT with the greatest involvement of the CA1 and subiculum regions [75]. Previous subfield volumetric studies have documented the greatest severity of atrophy in the CA1 region [73], deformation of the hippocampal head, [74] and sparing of the posterior hippocampus [76].

1.4 Hippocampal Segmentation

1.4.1 Manual Segmentation

Hippocampal subfield volumetry has been extensively studied in patients with MCI and AD. In histology, hippocampal subfields are defined based on neuroanatomical features (i.e. transitions in cytoarchitecture) [70]. Manual segmentation of MR images can identify atrophy of specific hippocampal subfields due to neurodegenerative disorders such as AD [77]. Manual segmentation entails manual tracing of hippocampal subfield boundaries of the hippocampus on MR images [78]. However, manual hippocampal subfield volumetry has several important limitations. The first limitation is that manual segmentation is labor and time intensive [78,79]. The second limitation is that there are a large number of different manual segmentation protocols previously described in the literature, the vast majority of which are not histologically validated [80]. This makes the comparison of results across different laboratories problematic.

1.4.2 Automated Segmentation Software

Many automated segmentation programs have previously been developed to overcome the limitations of manual segmentation protocols described above. These tools provide automated segmentation of MRI images to segment the hippocampus into its constituent subfields. A variety of methods have been described, including machine learning approaches based on 'ground truth' manual segmentation of hippocampal subfields [81]. In contrast, other previous methods in the literature have utilized a multi-atlas approach to describe probabilistic segmentation of MRI images [81].

Some notable software currently widely used in the previous literature include Freesurfer and Automatic Segmentation of Hippocampus subfield (ASHS). Freesurfer is an open-source

automated segmentation program that is used to analyze and visualize brain anatomy. Freesurfer uses a single probabilistic atlas for its segmentations and it assigns labels depending on alignment with the atlas probability along with image intensity [82].

ASHS is another well-known automated segmentation program that uses a slightly different approach than Freesurfer. ASHS uses a multi-atlas segmentation technique which consists of a training pipeline and then later a segmentation pipeline. In this method, the training pipeline is based on one set of subjects to create a segmentation multi-atlas package, and this package is later used for the segmentation of new subjects [83].

1.4.3 Limitations

Freesurfer, ASHS, and other automated segmentation have limitations to them that prevent research to localize atrophy patterns beyond that of whole hippocampus volumes and whole subfield volumes. First, current automated segmentation programs do not fully segment subfields throughout the entire anterior-posterior axis of the hippocampus (head, body, and tail) [84]. The tail and head of the hippocampus have very curved anatomy making it difficult for certain automated segmentation programs to segment along the entire long axis, which leads to subfield discontinuity [85]. Furthermore, existing methods (ASHS and FreeSurfer) do not allow for hippocampi to be aligned in a common space, which makes a comparison of atrophy patterns across patients and correlation with existing biomarkers technically difficult.

1.4.4 HippUnfold

HippUnfold is an automated segmentation program that uses U-net learning (described below) to take into account the variable folding patterns of the hippocampus, including the head and the tail of the hippocampus, and segments the subfields through the long axis of the hippocampus [86]. By unfolding the hippocampus into flat maps in a common space - this software can give us localized insights into the atrophy patterns of the hippocampus. This includes thickness and volumetric profiles of the subfields of the hippocampus with regional specificity. This is achieved by using continuous subfield labeling throughout the head, body, and tail which can be correlated with existing biomarkers using a recently developed tool called BrainStat [87]. HippUnfold has the ability to not only calculate subfield volumes, but it has the ability to

measure the thickness of the hippocampus throughout the entire anterior-posterior axis of the hippocampus, something not seen with conventional automated software.

1.5 Research Hypothesis

Here we aimed to use two recently developed tools (HippUnfold and BrainStat) to correlate hippocampal thickness measurements on a vertex-wise basis with tau PET values. We hypothesized that a decrease of hippocampal thickness values, especially in the subiculum and CA1 would be correlated with increase in tau PET in a cohort of healthy elderly, patients with MCI, and patients with AD.

Chapter 2. Methods

2.1 Alzheimer's Disease Neuroimaging Initiative (ADNI)

2.1.1 Background and Cohorts

Data used for this study was obtained from the Alzheimer's Disease Neuroimaging Initiative (ADNI) database (adni.loni.usc.edu), led by Principal Investigator Michael W. Weiner, MD.

ADNI was launched in 2004 as a longitudinal multicenter study that encompasses clinical, imaging, genetic, and biochemical biomarkers for the early detection and tracking of the progression of AD and to assess the brain structure and function over the course of the disease [88]. ADNI is an open-source database that enables the sharing of data between researchers around the world. From the time of its launch, ADNI has gone through multiple phases consisting of different goals, acquisition criteria, patients, and objectives. ADNI enrolls patients between the ages of 55 and 90 across the United States and Canada [88]. ADNI is a large database acquired from healthy elderly patients, subjects with MCI, and AD and includes a wide range of patient data including cognitive scores (MMSE and MoCA), medication data, vital signs, neurological exam scores, demographic information, genetic data, cerebral spinal fluid biomarkers, and imaging biomarkers such as MRI and PET.

As part of our inclusion criteria, all patients had at least one Highreshippocampus (high resolution T2 weighted) image taken at any visit during the study. All patients also had full

cognitive score profiles that include MMSE and MoCA. Finally, all patients had full PET phosphorylated tau profiles. This includes SUVRs for the METAROI, the Inferior Temporal region, and the Entorhinal region. Patients who had these criteria listing were included in this study.

2.1.2 Imaging Biomarkers

The high resolution T2-weighted images were acquired with an oblique orientation - with 2mm thick slices perpendicular to the long axis of the hippocampus, with a spatial resolution of: 0.39 x 0.39 x 2 mm [89]. These images were acquired from ADNI 3 and from roll over patients from ADNI 2 who were reassessed in ADNI 3. All images were acquired through a 3T scanner. The timing parameters include repetition time (TR) of 8020 ms and a time of echo 50 ms. T2 weighted images were used due to its ability to detect diseases and neuropathological processes [90].

These images were used in our segmentation software to calculate the volume and thickness of subfields throughout the long axis of the hippocampus. T2 weighted images were assessed to ensure adequate visualization of the hippocampus prior to inclusion in our study.

2.1.3 Positron Emission Tomography Biomarkers

PET biomarkers were also analyzed for this project. AV1451, also known as Flortaucipir, was used to detect abnormally phosphorylated tau (tau PET). Here we look at three different regions of interest while keeping the reference region as the inferior cerebellar region the same when calculating the SUVRs for all the regions. The first region of interest is the METAROI which is comprised of the bilateral entorhinal cortex, amygdala, fusiform gyrus, and inferior and middle temporal cortices. The second region of interest is the inferior temporal cortex region. Finally, the last region of interest is the entorhinal region of interest. The entorhinal cortex indicates early tau deposits, while the inferior temporal region is affected later in AD, and METAROI encompasses a broader area of tau deposits. By analyzing these three regions we endeavoured to encompass the spectrum of potential tau burden seen in patients with AD. In this study, we used continuous tau PET data instead of discrete cut-off thresholds to define tau positivity. In

summary, we compared tau PET as a continuous variable to hippocampal thickness (also a continuous variable) in order to characterize the relationship between these two measures.

2.1.4 MRIcroGL and Brain Imaging Data Structure (BIDS) Formatting

MRIcroGL software is used to convert the DICOM files of each downloaded folder into a NIFTI file. Next, individuals were organized under Brain Imaging Data Structure (BIDS) formatting, an organizing scheme used by neuroscientists. Due to there being an increase in neuroimaging analysis, BIDS formatting was created as a universal organization of neuroimaging data used by data scientists and researchers in the field of image analysis as a universal and organized way to interpret data [91]. HippUnfold is a BIDS app, that uses and understands BIDS datasets. BIDS apps require the input files to be formatted in a particular way for the program to read the input data appropriately and compute the desired output measurements.

2.2 HippuUnfold

2.2.1 Background:

HippUnfold is a recently released automated segmentation software that works with T1-weighted or T2-weighted MR images to segment the subfields along the long axis of the hippocampus and renders the volume, thickness values, and other parameters of hippocampal subfields [86]. As discussed above, HippUnfold was created to overcome some of the limitations of current automated hippocampal segmentation programs, specifically to consider and accommodate the variability of size, shape, and folding patterns seen across hippocampi. HippUnfold employs a "U-net" deep convolution neural network and enforces topological constraints on the hippocampus. U-net is a deep learning architecture that was trained and tested on 738 hippocampal MR images from 369 subjects in the human connectome project [86]. The neural network segments the grey matter along with the stratum radiatum, lacunosum, and moleculare (SRLM), and structures surrounding the hippocampus. It does so accurately due to the high number of subjects used in the training phase of the program and has also been generalized to other datasets. HippUnfold training was repeated using T1-weighted, T2-weighted, and diffusion weighted images. Once U-net segments the hippocampus appropriately, it defines consistent and specific boundaries of the hippocampus. From these boundaries, Laplacian equation is applied and solved to create a geodesical coordinate gradient so that each

hippocampus in this study has the same intrinsic surface alignment. Each coordinate number created from the Laplacian equation is defined as a vertex and these vertices can be used for statistical comparisons. Hippocampi are subsequently 'unfolded' and co-registered into common space using the same boundaries segmented from the U-net program.

2.2.2 Laplacian Equation

The Laplacian equation is initially a mechanical engineering term used in the past to describe heat transfer. The concept can be described with the example of utilizing two points, one being very hot and one being very cold [92]. Laplacian equation is used to create a gradient between the very hot point to the very cold point. An example of this can be seen in Figure 2a) The very hot point is labeled as +9.0 while the very cold point is labeled as -9.0. 2b) then applies the Laplacian equation to create a gradient between the very hot point and the very cold point to fill in the rest of the grid. This is what HippUnfold employs after the U-net segments the hippocampus and uses surrounding structures to create the unfolded flat map space boundaries.

The example given by DeKraker et al. in HippUnfold is that if you imagine a wire attached to something very hot (100 degrees) and then something very cold (0 degrees) and wait for the wire to reach equilibrium. You then have another wire that can be of different lengths (mimicking the variability of the hippocampus) and let that second wire reach equilibrium. To allow comparison of these two wires, one would find a homologous point between the two wires which are at the same temperature after equilibrium - and compare these two points (e.g. where both of the wires are at '10 degrees'). This is the same concept used to the segment the hippocampus with HippUnfold. First U-net defines boundaries, and then the Laplacian equation creates a gradient between the two boundary points. To find two homologous points between two different hippocampi, we would look for a value created by the Laplacian equation we are interested in. For example, if a certain gradient number to another certain gradient number encompasses the subiculum of the hippocampus, any gradient number between those points that we choose would be homologous between all hippocampi and would be located in the subiculum. This principle underlies how HippUnfold places hippocampi of varying shape and size into spatial correspondence via Laplacian coordinate systems [86].

After U-net segmentation, there are 3 axis boundaries the HippUnfold uses. The first one is the anterior-posterior axis. The Laplacian field in HippUnfold is created by marking the

anterior boundary of the hippocampus as 0 and the posterior part of the hippocampus as 1. The Laplacian equation then creates a geodesic coordinate gradient between these two boundary points. The next boundary point is the proximal (proximal to the adjacent temporal lobe, i.e. the subiculum) -distal (distal to the adjacent temporal lobe, i.e. the DG) axis with one of the boundaries labeled as 0 and the other labeled as 1 with the Laplacian equation creating a gradient between these two boundaries. Now this creates a rectangle that has a full coordinate gradient plane spanning the 2D dimensions of the entire hippocampus flat rectangle. A third coordinate gradient is then added encompassing the interior to outer axis (IE laminar), and this axis generates the thickness axis of the hippocampus. From these three axes, the Laplacian equation creates a gradient coordinate grid throughout the entire hippocampus in three dimensions. The gradient numbers now can be described as vertices on the hippocampal surface. This creates an intrinsic alignment between all the hippocampi in this study, as the vertices in the unfolded flat map for each hippocampus will match the corresponding vertices on all other hippocampi. This makes it possible to perform statistical analysis on all the hippocampi in the study due to this intrinsic alignment of vertices created by the Laplacian equation. In conclusion, from the Laplace coordinates spanning over the entire hippocampus, these surfaces have corresponding vertices which allows for registration between individuals.

Figure 2.

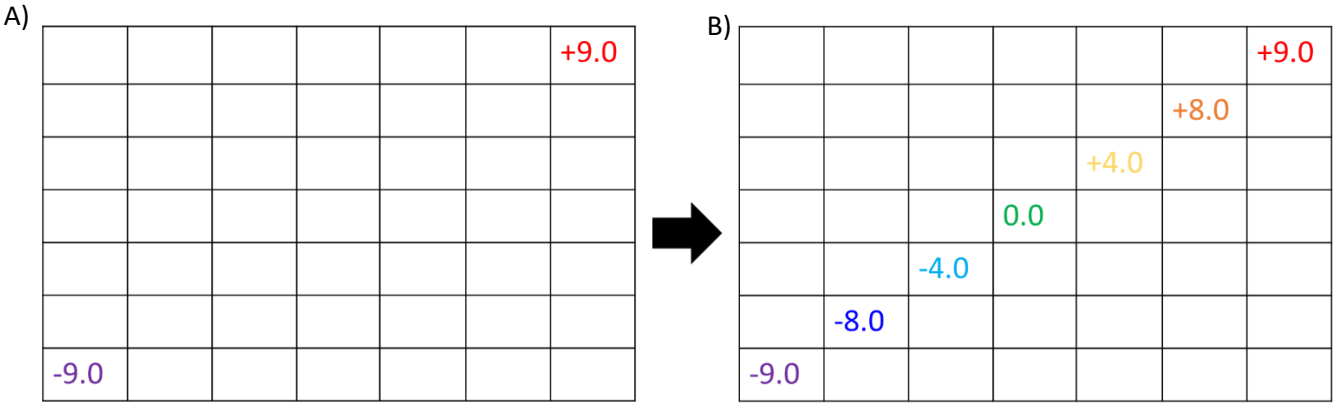

Figure 2. Diagrammatic explanation of Laplacian equation.

A) A hypothetical grid is displayed, the extremes of which have values of -9.0 (cold, purple) and +9.0 (hot, red), and are shown in the corners of the grid.

B) Laplacian equation is applied to create a coordinate grid between these two points of known value. From this, we get known values between the two initial points of interest.

2.2.3 BigBrain labels and Flatmaps

Once the flat maps are constructed by HippUnfold and the entire Laplacian coordinate gradient is created, there is an intrinsic alignment between all of the hippocampi which allows for comparison between any two points of interest (as described in the '10 degrees' analogy above). The last step HippUnfold does is topologically constrain the hippocampus. The program employs a surface based-subfield boundary segmentation, which is based on MR-identifiable features and validated against manual segmentation of BigBrain 3D histology, to produce unfolded flap maps of the hippocampus [86]. By utilizing this method, all hippocampi in our study also have corresponding subfield labeling spanning the entire anterior-posterior axis of the hippocampus (i.e subfields are placed into spatial correspondence). HippUnfold thus uses a topologically constrained framework which helps overcome the limitations of the current segmentation programs used in current hippocampal subfield research [86]. This method uses the Laplacian coordinate framework, HippUnfold flatmaps, along with topologically constrained subfields in order to enable comparison across large number of hippocampi of different size and shape.

2.2.4 HippUnfold vs Other Automated Segmentation Software

As described above, our rationale for using HippUnfold over other existing automated segmentation software relates to the limitations that it overcomes, specifically the inability of existing programs to account for the variability of the different size, shape, and folding patterns between individual hippocampi. This is because current automated segmentation software such as Freesurfer and ASHS employ single atlas or multiple atlas fusion templates when segmenting MR images. A limitation of this approach is that it does not fully capture the variability displayed in the hippocampus between different individuals and the different folding patterns between individuals. Relatedly, one of the biggest limitations of current software is the inability to fully segment all subfields throughout the entire anterior-posterior axis of the hippocampus (head to the tail). Illustrative examples include that these software programs can result in oversimplifications such as the anterior part (head) of the hippocampus being labelled exclusively as CA1, or omissions such as the posterior region (tail) can remain unlabelled [86]. In

addition, current approaches can result in discontinuity of hippocampal subfields throughout the long axis.

Finally, HippUnfold is able to generate quantitative metrics of hippocampal structure – which cannot be easily analyzed with existing tools. Hippocampal thickness is a parameter related to hippocampal volume, but which could provide greater insights to long axis hippocampal atrophy in comparison to volumes. As HippUnfold produces flatmaps, it allows analysis of the hippocampus as a ribbon (in its unfolded form) such that the thickness can be readily calculated, measuring from the inner to the outer surfaces.

2.2.5 Key Outputs

Figure 3 below shows the output of HippUnfold - with hippocampal subfields segmented in the coronal, sagittal, and axial planes. From these segmented subfields, important parameters are extracted including: thickness (mm), gyrification, and curvature.

Figure 3.

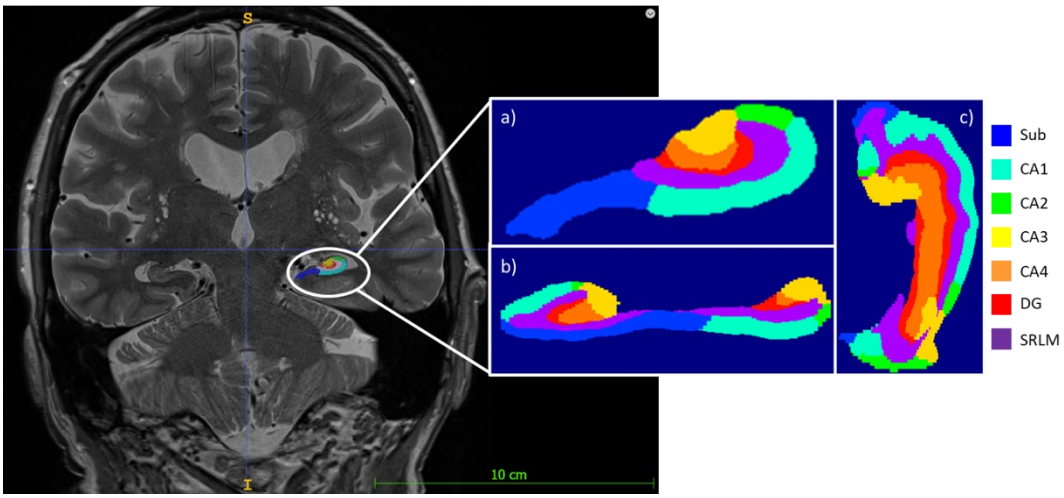

Figure 3 - Subfield volumetry throughout the entire hippocampal long axis with HippUnfold

Coronal High resolution (2mm slice thickness – 0.39x2x0.39mm) T2-weighted MR Image is shown at the level of the hippocampal body. HippUnfold-based subfield delineations are shown for the left hippocampus in the a) coronal, b) sagittal, and c) axial planes yielding subfield

volumes for Sub= Subiculum, CA = Cornu Ammonis, DG = Dentate gyrus and SRLM=stratum radiatum, Lacunosum, and moleculare.

From HippUnfold we are able to obtain volume outputs of the subfields in mm^3 of the left and right hippocampi and we are also able to acquire thickness measurements. As discussed above, HippUnfold produces a Laplacian coordinate grid with 14,000 vertices per subject, the first 7000 being from the left hippocampus and the other 7000 being from the right hippocampus. Finally, the surface labels of the unfolded surface are obtained. The images and segmentation were quality checked to make sure that HippUnfold did a proper and thorough scan of the MRI images and an anatomically reasonable segmentation of hippocampal subfields. Quality check was done via the quality check output file where you are able to visualize the segmentations and labels along with the 3D rendering of the hippocampus.

2.3 BrainStat

2.3.1 Background

Python is a universal coding language that is an open-sourced program that allows data scientists to use pre-made and built-in user packages in their analysis. Jupyter notebook was used as the integrated development Environment (IDE) used for the analysis of the project. Important Python packages that were downloaded included BrainStat, HippUnfold_toolbox, Brainspace, Nilabel, Pandas, Numpy, Matplotlib.pyplot and Glob. The code used for this project can be found at https://github.com/MujtabaSiddique/ADNI, which outlines the multiple packages we used to run the statistical models. BrainStat was used for the statistical analysis of linear regression models and Hippunfold_toolbox was used for the plotting of the images.

Thickness files were smoothened to 2mm as smoothening is required as an assumption for the statistical analysis performed in our study (random field theory). Smoothened thickness data for all the individuals in the study were merged and averaged out for both the left and right hippocampi separately. BrainStat SLM (general linear model) package was then used to apply linear regression models on a vertex-wise basis to test for significant correlation between our two variables of interest: 1) tau PET SUVRs and 2) hippocampal thickness [87] and to evaluate for statistically significant peaks and clusters. Finally, the significant clusters and peaks between

these two variables were plotted in common space on the flatmaps generated in the Hippunfold toolbox.

2.3.2 Linear regression model

The linear regression model used in BrainStat is modeling a relationship between two or more variables by fitting a linear equation to the observed data. This is used to model the relationship between a dependant variable, whether it be brain activity or brain thickness to other predictors or independent variables. General linear models follow the equation $Y = XB + Z\gamma + e$, where Y is the n-m matrix (n is the number of subjects and m is the number of vertices), B and γ are model coefficients. X and Z are the fixed or random effect predictors and e is the error [87].

In our study, the predictors used such as age, sex, diagnostic group, and tau PET levels, were classified as fixed effects in the linear model [93]. This was decided based on the fact that in this study, we were primarily interested in examining only the relationship between tau PET and hippocampal thickness values, and random effects were not expected to contribute significantly to the variability in either of these two measurements[94]. Tau PET was the contrast vector when correlating it with the decrease in hippocampal thickness and the linear model was performed as a one-tailed t-test when conducting our regressions.

2.3.3 Statistical Analysis

This study uses ordinary least squares (OLS) to estimate the model coefficients. Since our model only contains fixed effects, BrainStat solves the ordinary least square (OLS) problem for each brain location [87]. OLS is a method that is commonly used for fitting linear regression models to a set of data points to understand a relationship between a dependent variable (in this case hippocampal thickness) and independent variables (in this case tau PET SUVR) [95]. The goal of the ordinary least square problem is to best fit the data by minimizing the sum of square differences, to reduce the errors between the actual values and the predicted values of the dependent variable at each vertex.

In this study, the test to compute the t-statistics is a student t-test. A t-test is used to test for the significance of the estimated coefficients of the independent variables to determine if there is a relationship between the dependant and independent varible. The t-statistics are then

used to derive the p-values to determine if a significant relationship is developed [96]. Due to the high number of multiple statistical tests being conducted on our data, multiple comparison tests are also performed in BrainStat to reduce the number of false positives errors in our results, because as one performs multiple statistical tests, the probability of obtaining a statistically significant result increase, so the aim of this is to control for that so no erroneous conclusions are made from the statistical tests. The two multiple comparisons tests used in this study are the false discovery rate and random field theory. Random field theory corrects for the probability of ever reporting a false positive [97]. The basis behind random field theory is that it is a statistical test that tests whether the observed data deviates significantly from what would be expected if the data was completely random. As discussed, smoothening is one of the assumptions required for random field theory. False discovery rate is another multiple comparison test employed in our study to mitigate the likelihood of false positives in the data.

2.3.4 Significant Clusters and Significant Peaks

It is important to define a significant cluster and a significant peak and what they mean from a statistical analysis point of view. Significant clusters in a certain area indicates that a cluster group of adjacent vertices meet and exceed a provided threshold of magnitude and size. Significant clusters in other terms are defined by a group of adjacent vertices that show a statistically significant difference in mean thickness. Significant clusters provide us with information about the spatial extent and distribution of brain regions affected. If there are only significant clusters available that suggests that increase tau PET effects cover a large region rather than local foci. Significant clusters show broader regions of interest. Signficant clusters are calculated by setting a cluster defining threshold, $p = 0.01$. Significant peaks in a certain cluster indicates that the statistical significance of individual vertices peaks within a cluster has the highest magnitude of correlation between reduced thickness and increase abnormal tau deposits. It is a measure of significance of individual peaks within clusters that contribute most strongly to the observed results. Significant peaks provide information about specific focal regions within the clusters where the effects and correlation are strongest. Peaks are calculated individually via t-test in regression models.

Figure 4.

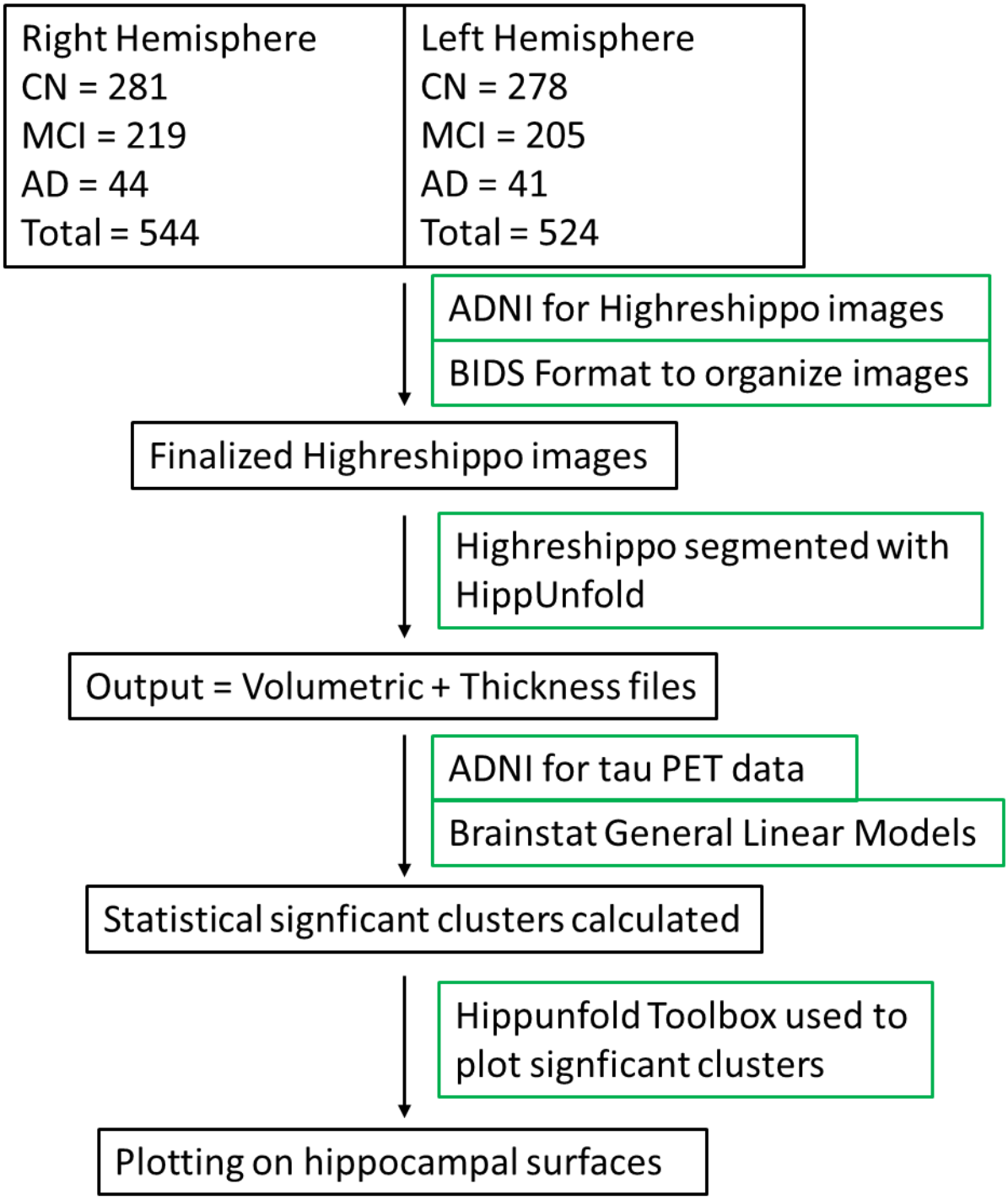

Figure 4 – Methodology of hippocampal subfield thickness correlations

High resolution MR images (0.39x2x0.39mm) were obtained for subjects (CN, cognitively normal; MCI, mild cognitive impairment; AD, Alzheimer's Disease) from the ADNI database

and processed using Brain Imaging Data Structure (BIDS) formatting, a universal way for organizing neuroimaging data. HippUnfold was then used to provide automated segmentation of individual hippocampal subfields – yielding subfield volume and thickness measurements. Tau PET values were then correlated with thickness data using the BrainStat general linear model package to identify significant clusters and peaks on the hippocampus – which are then plotted on hippocampal flatmaps using the HippUnfold toolbox.

Chapter 3. Results

3.1 Demographics

In this study, patients were separated into both left-hemisphere hippocampus and right-hemisphere hippocampus cohorts. This was done so that the appropriate thickness values for each hemisphere were plotted on their appropriate left or right flatmap for statistical analysis purposes. We also have left and right cohorts because certain patients in ADNI had properly segmented left hippocampus but very atrophic right hippocampus, while others had properly segmented right hippocampus and atrophic left hippocampus that could not be appropriately segmented. In order to use all of the properly segmented hippocampi, the patient cohort was split into left and right hemispheres with the majority of the patients being in both cohorts.

The baseline demographic details for the left hemisphere cohort are seen in Table 1. A total of 524 patients had HippUnfold segmented left hippocampi that were acquired from the ADNI 3 database. For the cognitively normal cohort, the mean age was 71.6 ± 7.4 years while the mean age for the MCI and AD group were 73.0 ± 7.6 years and 73.6 ± (8.7) years respectively. The number and percentages of females in all three groups from CN, MCI to AD groups were 169(60.8%), 95(46.3%), and 17(41.5%). The average MMSE scores for the CN, MCI, and AD groups are 29.0 ± 1.3, 27.9 ± 2.0, and 23.4 ± 3.2. The average MoCA scores for the CN, MCI, and AD groups are 26.1 ± 2.6, 23.4 ± 3.4, and 17.6 ± 4.7. The mean standard uptake volume ratio for the METAROI region increases from 1.20 ± 0.11 in the CN group to 1.30 ± 0.28 in the MCI group and finally 1.61 ±0.37 in the AD group. This increase in the SUVR is also seen in the Entorhinal cortex with 1.15 ± 0.12 in the CN group to 1.27 ± 0.27 in the MCI group and finally 1.51 ± 0.25 in the AD group and the Inferior temporal cortex with 1.23 ± 0.15 in the CN group to 1.33 ± 0.33 in the MCI group and finally 1.70 ± 0.47 in the AD group.

The demographics for the right hemisphere cohort were comparable as seen in Table 2. A total of 544 patients had fully segmented right hippocampi that were acquired from the ADNI database. For the cognitively normal cohort, the mean age was 71.6 ± 7.3 years while the mean age for the MCI and AD group were 73.7 ± 7.8 years and 74.0 ± 8.9 years respectively. The number and percentages of females in all three groups from CN, MCI to AD groups were 172(61.2%), 103(47.0%), and 20(45.5%). The average MMSE scores for the CN, MCI, and AD groups are 29.0 ± 1.3, 27.7 ± 2.2, and 22.8 ± 3.6. The average MoCA scores for the CN, MCI, and AD groups are 26.1 ± 2.6, 23.2 ± 3.5, and 17.3 ± 4.9. The mean standard uptake volume ratio for the METAROI region increases from 1.20 ± 0.11 in the CN group to 1.30 ± 0.28 in the MCI group and finally 1.63 ± 0.38 in the AD group. This increase in the SUVR's is also seen in the Entorhinal cortex with 1.15 ± 0.12 in the CN group to 1.28 ± 0.27 in the MCI group and finally 1.53 ± 0.24 in the AD group and the Inferior temporal cortex with 1.21 ± 0.12 in the CN group to 1.33 ± 0.31 in the MCI group and finally 1.68 ± 0.44 in the AD group.

Table 1. Patient Demographics

a)

Variable	Cognitively Normal (n=278)	Mild Cognitive Impairment (n=205)	Alzheimer's Disease (n=41)
Sex Female, n (%) Male, n (%)	 169 (60.8) 109 (39.2)	 95 (46.3) 110 (53.7)	 17 (41.5) 24 (58.5)
Mean age, years (SD)	71.6 (7.4)	73.0 (7.6)	73.6 (8.7)
Mean MMSE score (SD)	29.0 (1.3)	27.9 (2.0)	23.4 (3.2)
Mean MoCA score (SD)	26.1 (2.6)	23.4 (3.4)	17.6 (4.7)
Mean Tau PET METAROI SUVR (SD)	1.20 (0.11)	1.30 (0.28)	1.61 (0.37)
Tau PET Entorhinal Cortex Mean LH SUVR (SD) Mean RH SUVR (SD)	 1.15 (0.12) 1.15 (0.12)	 1.27 (0.27) 1.28 (0.28)	 1.51 (0.25) 1.51 (0.24)
Tau PET Inferior Temporal Cortex Mean LH SUVR (SD) Mean RH SUVR (SD)	 1.23 (0.15) 1.21 (0.13)	 1.33 (0.33) 1.32 (0.32)	 1.70 (0.47) 1.67 (0.44)

b)

	Cognitively Normal (n=281)	Mild Cognitive Impairment (n=219)	Alzheimer's Disease (n=44)
Sex Female, n (%) Male, n (%)	 172 (61.2) 109 (38.8)	 103 (47.0) 116 (53.0)	 20 (45.5) 24 (54.5)
Mean age, years (SD)	71.6 (7.3)	73.7 (7.8)	74.0 (8.9)
Mean MMSE score (SD)	29.0 (1.3)	27.7 (2.2)	22.8 (3.6)
Mean MoCA score (SD)	26.1 (2.6)	23.2 (3.5)	17.3 (4.9)
Mean Tau PET METAROI SUVR (SD)	1.20 (0.11)	1.30 (0.28)	1.63 (0.38)
Tau PET Entorhinal Cortex Mean LH SUVR (SD) Mean RH SUVR (SD)	 1.15 (0.12) 1.15 (0.12)	 1.27 (0.26) 1.28 (0.27)	 1.53 (0.25) 1.53 (0.24)
Tau PET Inferior Temporal Cortex Mean LH SUVR (SD) Mean RH SUVR (SD)	 1.22 (0.14) 1.21 (0.12)	 1.34 (0.34) 1.33 (0.31)	 1.74 (0.51) 1.68 (0.44)

Table 1. – Patient Demographics

A) Left hemisphere B) Right hemisphere

The study population comprised three cohorts - Cognitively normal (CN), Mild Cognitive Impairment (MCI), and Alzheimer's Disease (AD). The proportion of females versus males in each cohort, age, MMSE, MoCA scores are displayed. Positron Emission Tomography (PET) phosphorylated tau SUVRs data are displayed from the regions of interest analyzed in our study.

3.2 Hippocampal Thickness Correlated to tau PET.

3.2.1 Meta-Temporal Region (METAROI).

The METAROI SUVR was correlated to the hippocampal thickness along the entire hippocampus. As mentioned briefly before, the METAROI consists of the bilateral entorhinal, amygdala, fusiform, inferior, and middle temporal cortices, all of which are areas affected by the abnormally phosphorylated tau tangles according to the proposed stages of tau pathology in AD. Linear regression models were run through BrainStat. In this linear regression model, the fixed effects included age, sex, age*sex interaction, diagnostic groups, and METAROI SUVR values. The contrast vector was METAROI which was fitted into the smoothened thickness values. There were significant clusters and significant peaks in the clusters throughout the hippocampus for both the right and left hemispheres. It can be seen that there are two significant clusters in the left hemisphere when decreased hippocampal thickness is correlated with tau PET SUVRs. Cluster 1 contained a total of 1920 vertices $p = 0.000003$ and is located in the body and the tail region of the subiculum and CA1 subfields of the hippocampus as seen in Figure 5. Cluster 2 in the left hemisphere contained 232 vertices, $p = 0.005791$, and is located in the body and tail regions of the CA4 and CA3 subfields. There are three significant clusters in the right hemisphere when correlating reduced hippocampal thickness to increase SUVR in the meta-Roi region. Cluster 1 in the right hemisphere contains 1383 vertices, $p = 0.000083$, and is located in the body and tail region of the subiculum and CA1 subfields as seen in Figure 5. Cluster 2 in the right hemisphere contains 317 vertices, $p = 0.004211$, is located in the head region of the CA1,

CA2, and CA3 subfields. Cluster 3 contains 145 vertices, p =0.025376, and is located in the body region of the CA3 and CA4 subfields.

As shown in Figure 6 - there are many significant peaks within the significant clusters that were seen in Figure 5. Looking at the 5 most significant peaks throughout the hippocampus, the peak with the strongest t-statistic and lowest p-value is located in cluster one p = 0.000003. The second and third most strongly correlated peaks were also located in cluster 1 with the p values of p = 0.000120 and p= 0.000821 respectively. Peak four and five had very high t-statistics as well and are located within cluster two with the p-values of p= 0.001275 and p = 0.008027 respectively. Significant peaks were also seen in the clusters of the right hemisphere. The strongest right hemisphere peak was found in cluster one with p = $1.4957 \times 10^{-9.}$ The next two significant peaks are located in cluster 2 with the p values of p = 2.192×10^{-3} and 2.967×10^{-3}.

Figure 5

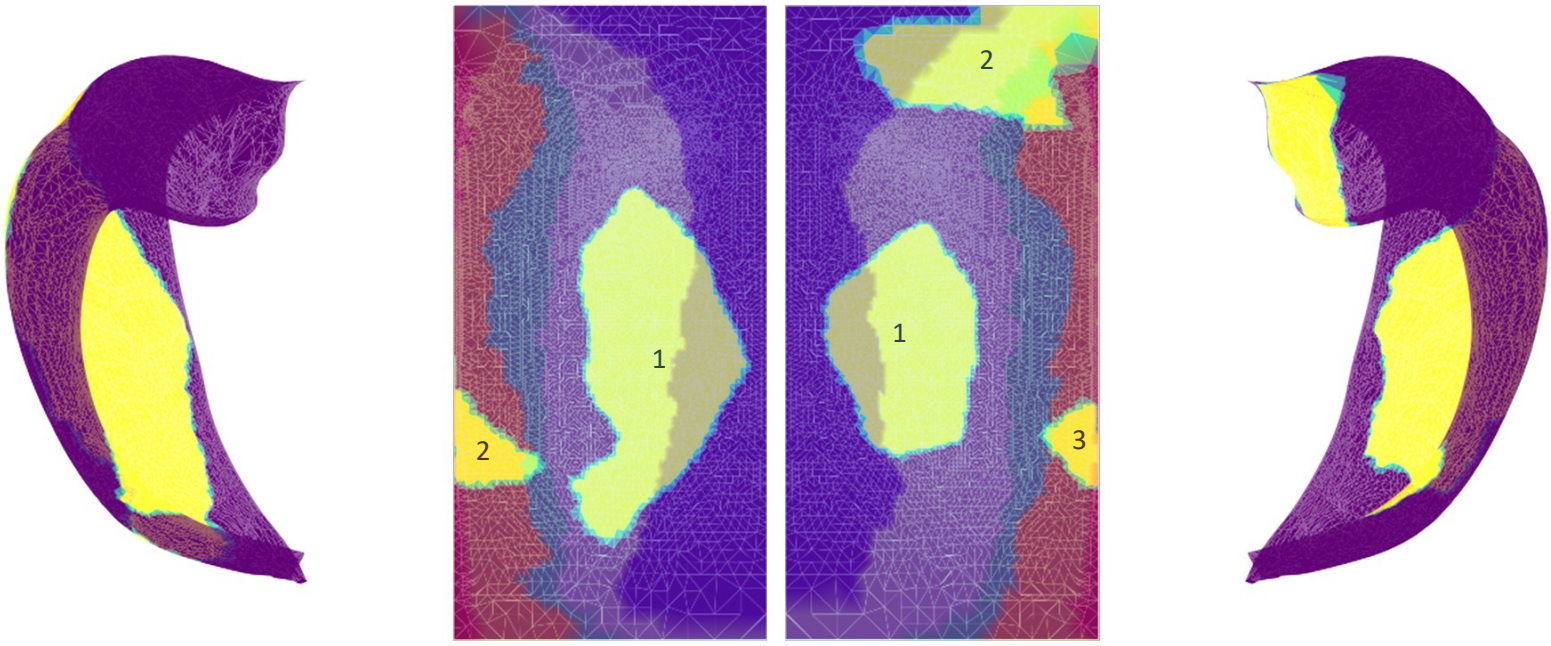

Figure 5. – Significant clusters when correlating METAROI PET tau to the reduced thickness

Significant clusters are produced by the linear regression model when comparing reduced hippocampal volume along the entire anterior-posterior axis to the SUVR values in the METAROI. Subfields were generated using the HippUnfold software from DeKraker et al. 2022 [86]. These BigBrain labeled subfields were then manually overlayed on top of the output flatmaps from BrainStat. The BigBrain labels are as follows, the blue is the subiculum, the aqua is the CA1, the green is the CA2, the orange is the CA3, and the red is the CA4 subfield. Cluster 1 in the left hemisphere is located in the body and the tail region of the subiculum and CA1. Cluster 2 in the left hemisphere is located in the body and tail regions of the CA4 and CA3 subfields. Cluster 1 in the right hemisphere is located in the body and tail region of the subiculum and CA1 subfields. Cluster 2 in the right hemisphere is located in the head region of the CA1, CA2, and CA3 subfields. Cluster 3 in the right hemisphere is located in the body region of the CA3 and CA4 subfields.

Figure 6

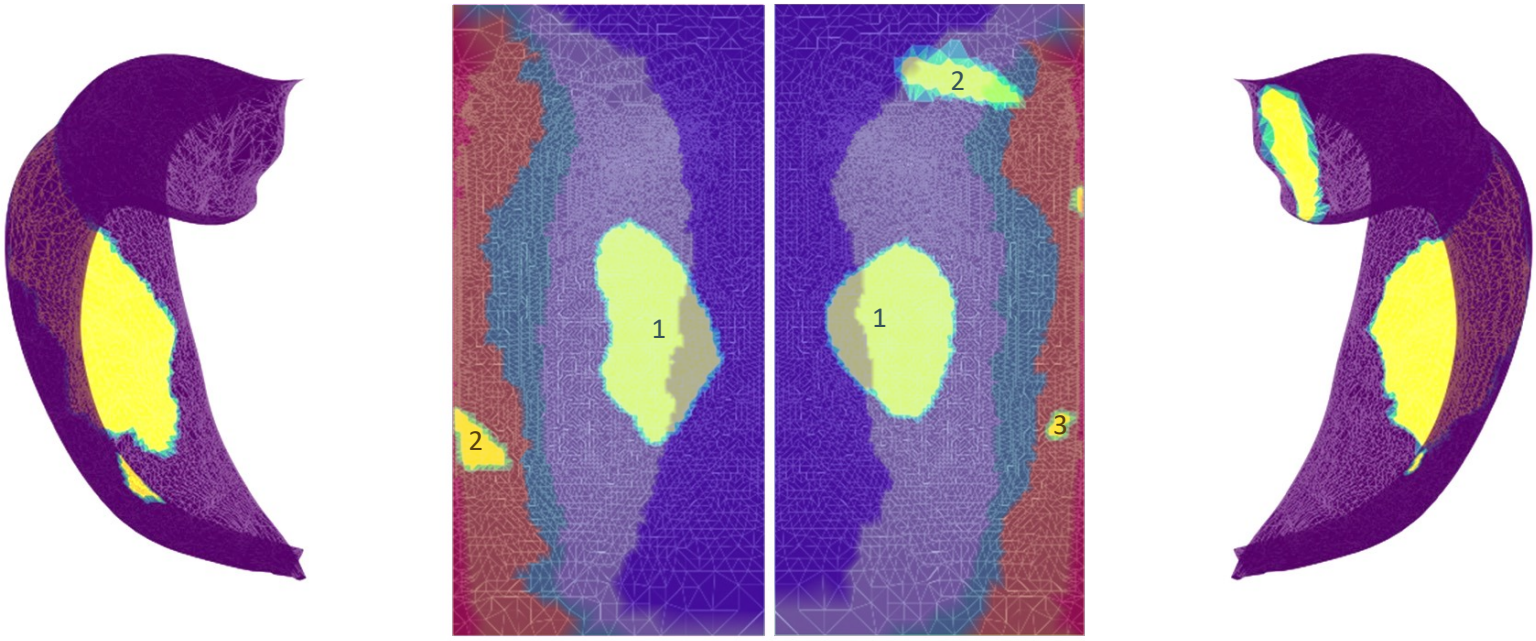

Figure 6 – Significant peaks when correlating METAROI tau PET to reduced thickness.
This figure shows significant peaks produced by the linear regression model when comparing reduced hippocampal volume along the entire anterior-posterior axis to the SUVR values in the METAROI. Significant peaks are plotted onto the hippocampal flatmap in both the right and left hemispheres and then it is folded back into its 3D conformation which can be seen by the images on either side of the flatmaps. Subfields were generated using the HippUnfold software from DeKraker et al. 2022 [86]. These BigBrain labeled subfields were then manually overlayed on top of the output flatmaps from BrainStat. The significant peaks are shown to be within significant clusters from Figure 5. Peaks are shown to be located in body of the subiculum, CA1, and CA3 subfields in the left hippocampus. The majority of the peaks are located in the body of the subiculum, CA1, and CA3 subfields as well as the head of the CA1-2 subfields in the right hemisphere.

3.3.2 Entorhinal Region.

The Entorhinal region SUVR was correlated to the hippocampal thickness along the entire hippocampus. The entorhinal cortex is a region in the brain that is one of the first sites of tau pathology seen in AD. Linear regression models were run through BrainStat. In this linear regression model, the fixed effects included age, sex, age*sex interaction, diagnostic groups, and entorhinal SUVR values. The contrast vector was entorhinal which was fitted onto the smoothened thickness values. There were significant clusters and significant peaks in the clusters throughout the hippocampus. Looking at the significant cluster values, it can be seen in the left hemisphere that there are four significant clusters. Cluster 1 contains a total of 2506 vertices, $p = 8.48 \times 10^{-8}$, and is located in the body and the tail region of the subiculum and CA1 subfields of the hippocampus as seen in Figure 7. Cluster 2 in the left hemisphere contained 203 vertices, $p = 7.15 \times 10^{-3}$, and is located in body regions of the CA2, CA3, and CA4 subfields. The third significant cluster contains 201 vertices, $p = 2.2 \times 10^{-2}$, which is located in the head region of the CA3 and CA4 subfields. There are three significant clusters in the right hemisphere when correlating reduced hippocampal thickness to increase SUVR in the Entorhinal region. Cluster 1 in the right hemisphere contains 1610 vertices, p = 0.000023, and is located in the body and tail region of the subiculum and CA1 subfields as seen in Figure 7. Cluster 2 in the right hemisphere contains 325 vertices, p = 0.006265, and is located in the head region of the CA1, CA2, and CA3 subfields. Cluster 3 contains 210 vertices, p =0.008943, and is located in the body region of the CA3 a d CA4 subfields.

As shown in Figure 8, many significant peaks are identified within the clusters that were significant in Figure 7. Looking at the 5 most significant peaks throughout the left hippocampus, the top three peaks with the strongest t-statistics and lowest p values are located in cluster one of p = 0000003, p = 0.00022, and p = 0.00142 respectively. Peaks 4 and 5 had very high t-statics as well and are located within cluster two with the p-values of p= 0.000477 and p = 0.000502 respectively. Significant peaks were also seen in the clusters on the right. The strongest right hemisphere peak is located in cluster one of $p = 1.0925 \times 10^{-7}$. The second strongest peak with the highest t-value and lowest p-value is located in cluster two of $p = 6.846 \times 10^{-4}$. The third peak is located in cluster three of $p = 2.29 \times 10^{-3.}$ The fourth peak is also located in cluster one like peak 1 with a $p = 3.74 \times 10^{-3.}$ Finally, the fifth peak is located in cluster two like peak one with a $p = 9.82 \times 10^{-3}$.

Figure 7

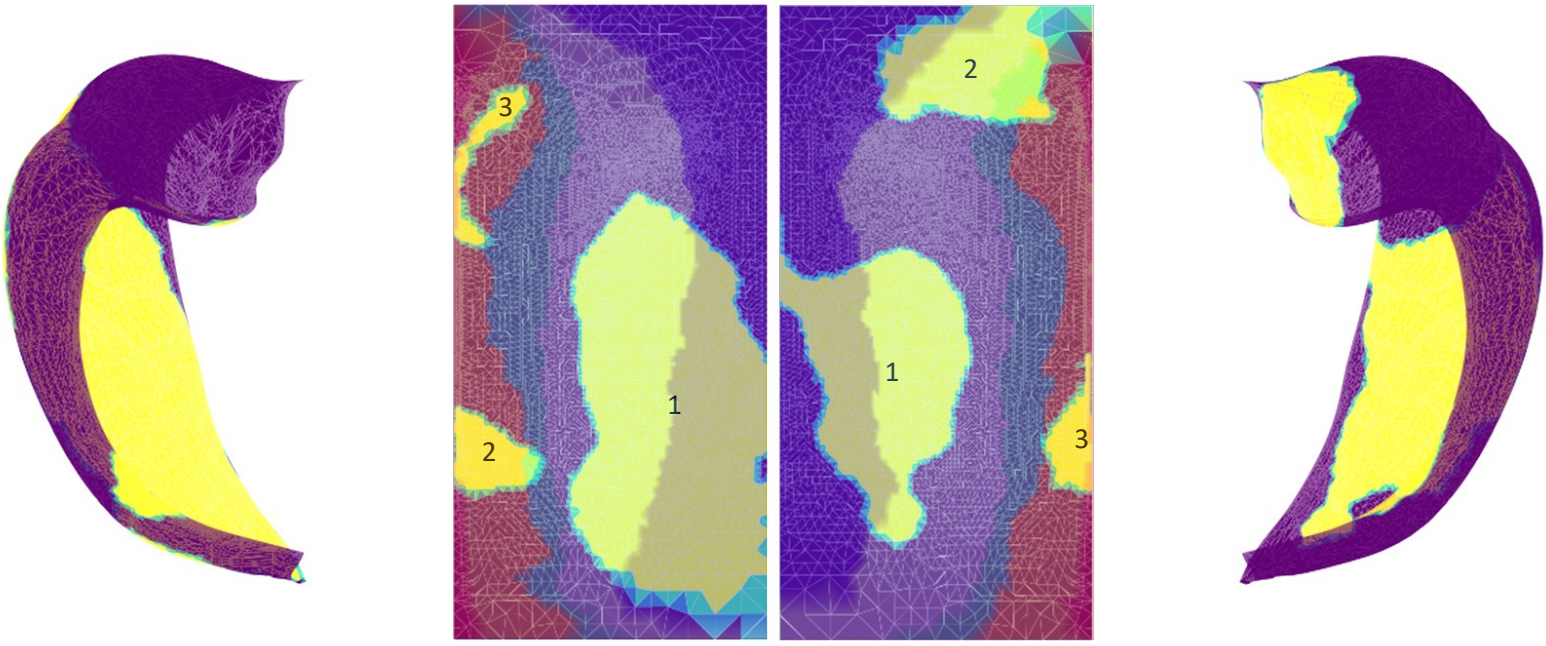

Figure 7– Significant clusters when correlating Entorhinal PET tau to reduced thickness.

This figure shows the significant clusters produced by the linear regression model when comparing reduced hippocampal volume along the entire anterior-posterior axis to the SUVR values in the Entorhinal. Subfields were generated using the HippUnfold software from DeKraker et al. 2022 [86]. These BigBrain labeled subfields were then manually overlayed on top of the output flatmaps from BrainStat. Cluster 1 in the left hippocampus is located in body and the tail region of the subiculum and CA1 subfields of the hippocampus. Cluster 2 in the left hemisphere is located in the body regions of the CA2, CA3, and CA4 subfields. Cluster 3 in the left hippocampus is located in the head region of the CA3 and CA4 subfields. Cluster 1 in the right hemisphere is located in the body and tail region of the subiculum and CA1 subfield.

Cluster 2 in the right hemisphere is located in the head region of the CA1, CA2, and CA3 subfields. Cluster 3 in the right hemisphere is located in the body region of the CA3 and CA4 subfields.

Figure 8

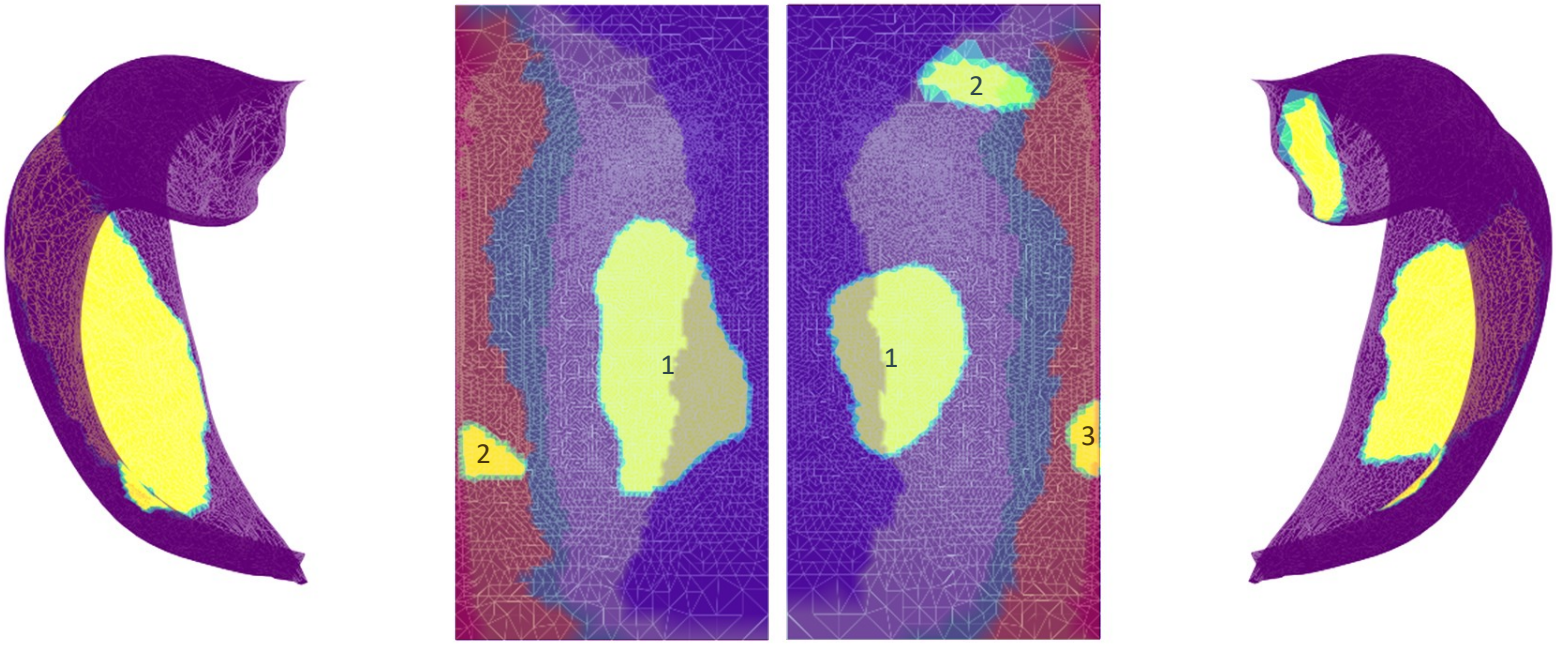

Figure 8 – Significant peaks when correlating Entorhinal PET tau to reduced thickness.

This figure shows the significant peaks produced by the linear regression model when comparing reduced hippocampal volume along the entire anterior-posterior axis to the SUVR values in the Entorhinal. Significant peaks are plotted onto the hippocampal flatmap in both the right and left hemispheres and then its is folded back into its 3D conformation which can be seen by the images on either side of the flatmaps. Subfields were generated using the HippUnfold software from DeKraker et al. 2022 [86]. These BigBrain labeled subfields were then manually overlayed on

top of the output flatmaps from BrainStat. These peaks were located in the clusters from Figure 7. Peaks are shown to be located in the body of the subiculum, CA1, and CA3 subfields in the left hippocampus. The majority of the peaks are located in the body of the subiculum, CA1, and CA3 subfields as well as the head of the CA1-2 subfields in the right hemisphere.

3.3.3 Inferior Temporal Region.

The Inferior Temporal region SUVR was correlated to the hippocampal thickness along the entire hippocampus. The inferior temporal region in the brain is one of the first sites of tau pathology seen in AD. Linear regression models were run through BrainStat. In this linear regression model, the fixed effects included age, sex, age*sex interaction, diagnostic groups, and Inferior temporal SUVR values. The contrast vector was inferior temporal which was fitted onto the smoothened thickness values. There are significant clusters and significant peaks in the clusters throughout the hippocampus.

Looking at the significant cluster values, it can be seen in the left hemisphere that there are three significant clusters in the left hemisphere when decreased hippocampal thickness is correlated with tau PET SUVR in the Inferior Temporal region. Cluster 1 contained a total of 1715 vertices, $p = 0.000012$, and is located in the body and the tail region of the subiculum and CA1 subfields as seen in Figure 9. Cluster 2 in the left hemisphere contained 178 vertices, $p = 0.0147$, and is located in the body and tail regions of the C3 and CA4 subfields. Cluster 3 contains 182 vertices, $p = 0.03813$, and is located at the head region of the CA3 and CA4 subfields. There are three significant clusters in the right hemisphere when correlating reduced hippocampal thickness to increase SUVR in the inferior temporal region. Cluster 1 in the right hemisphere contains 1181 vertices, $p = 0.000342$, and is located in the body region of the subiculum and CA1 subfields as seen in Figure 9. Cluster 2 in the right hemisphere contains 302 vertices, $p = 0.007984$, is located in the head region of the subiculum, CA1, CA2, and CA3 subfields. Cluster 3 contains 121 vertices, $p = 0.045744$, and is located in the body region of the CA4 subfield.

Figure 10 demonstrates many significant peaks within the clusters that were significant in Figure 9. The three peaks with the strongest t-statistics and lowest p values are located in cluster one: $p = 0.000573$, $p = 0.004140$, and $p = 0.004831$ respectively. Peaks 4 and 5 are located within cluster two with the p-values of $p= 0.006462$ and $p = 0.020878$ respectively. Significant

peaks were also seen in the clusters of the right hemisphere. The strongest right hemisphere peak was found in cluster one having a p-value of 1.4957×10^{-9}. The next two significant peaks are located in cluster 2 with the p values of $p = 2.192 \times 10^{-3}$ and 2.967×10^{-3}. Despite the cluster 4 not being significant, peak number 7179 in that cluster was significant showing $p = 1.43 \times 10^{-2}$ showing us significant in localization and not over a large region but rather a local foci.

Figure 9

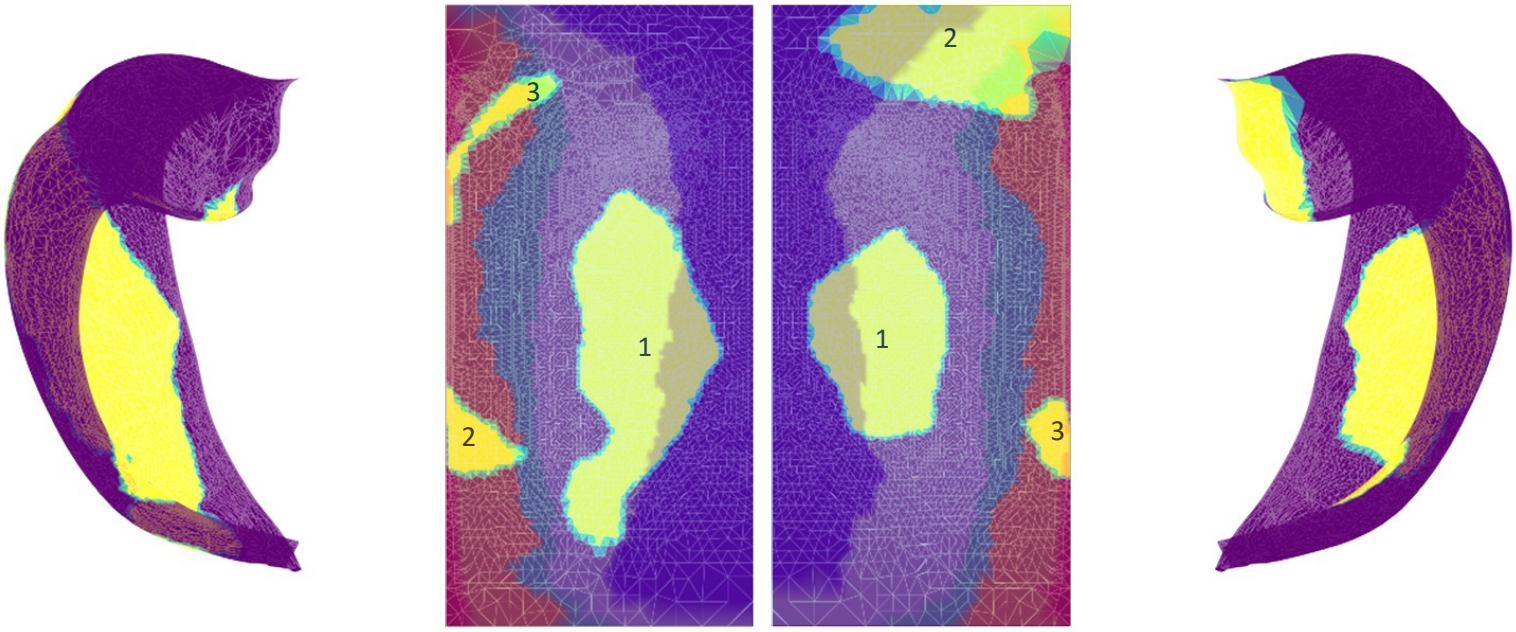

Figure 9. – Significant clusters when correlating Inferior Temporal PET tau to reduced thickness.

This figure shows the significant clusters produced by the linear regression model when comparing reduced hippocampal volume along the entire anterior-posterior axis to the SUVR values in the Inferior Temporal region. Subfields were generated using the HippUnfold software

from DeKraker et al. 2022 [86]. These BigBrain labeled subfields were then manually overlayed on top of the output flatmaps from BrainStat. Cluster 1 in the left hippocampus, is located in body and the tail region of the subiculum and CA1. Cluster 2 in the left hippocampus is located in the body and tail regions of the C3 and CA4 subfields. Cluster 3 in the left hippocampus is located at the head region of the CA3 and CA4 subfields. Cluster 1 in the right hippocampus is in the body region of the subiculum and CA1 subfields. Cluster 2 in the right hippocampus is located in the head region of the subiculum, CA1, CA2, and CA3 subfields. Cluster 3 in the right hippocampus is located in the body region of the CA4 subfield.

Figure 10

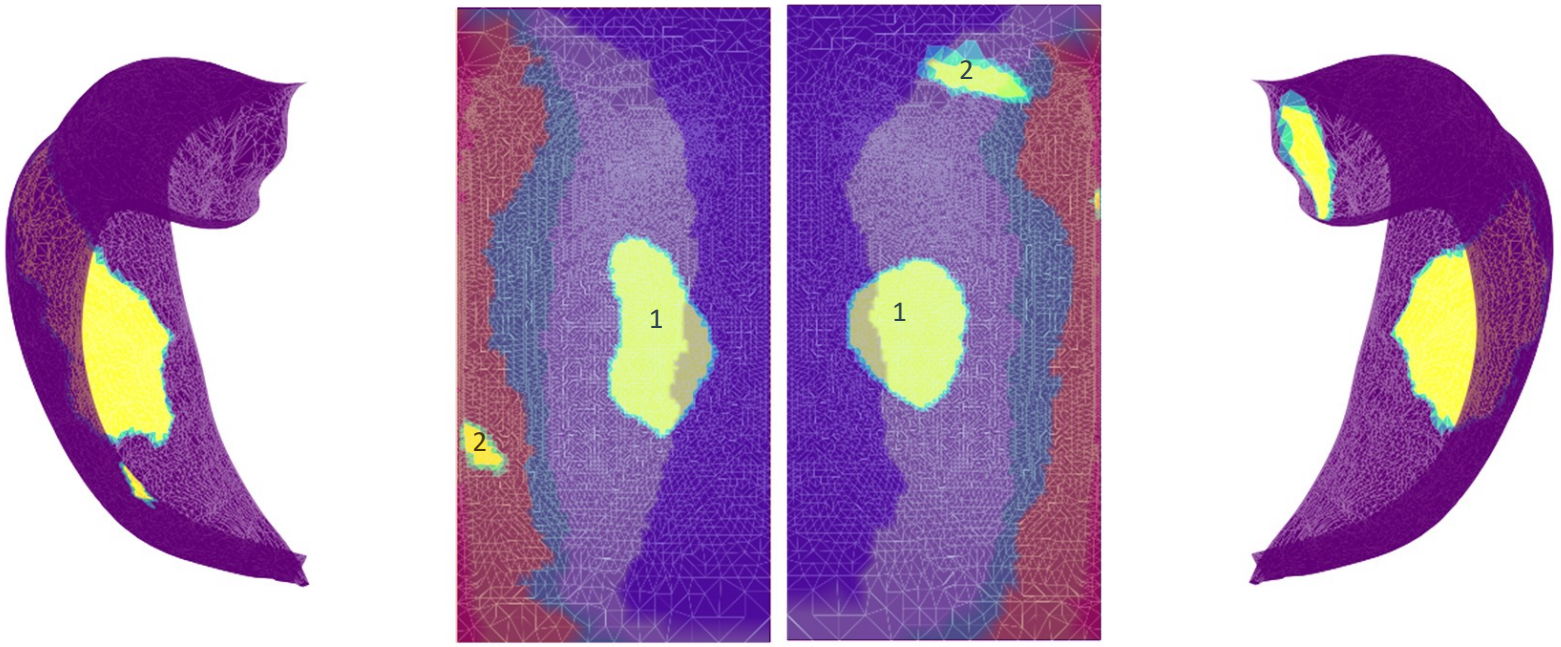

Figure 10. – Significant peaks when correlating Inferior Temporal PET tau to reduced thickness. This figure shows the significant peaks produced by the linear regression model when comparing reduced hippocampal volume along the entire anterior-posterior axis to the SUVR values in the Inferior Temporal region. Subfields were generated using the HippUnfold software from DeKraker et al. 2022 [86]. These BigBrain labeled subfields were then manually overlayed on top of the output flatmaps from BrainStat. Peaks are shown to be located in body of the subiculum, CA1, and CA3 subfields in the left hippocampus. The majority of the peaks are located in the body of the subiculum and CA1 subfields as well as the head of the CA1-2 subfields in the right hemisphere.

4. Discussion

4.1 Study Discussion

Accurate diagnosis of AD to allow for the selection of patients for clinical trials is important to test effective disease-modifying treatments for AD. Due to important limitations of clinical diagnosis of AD, biomarkers are increasingly used to supplement the clinical diagnosis of the disease in clinical trials [98]. Studies have shown tau PET biomarkers are better predictors of cognitive decline and episodic memory function in comparison to other biomarkers as pathological levels of tau in the brain when measured with PET tau imaging predicted a steeper decline in cognition longitudinally [52,51]. Despite tau PET biomarkers being able to detect abnormalities in the brain early on in the spectrum and being strongly correlated to clincal and cognitive symptoms of AD, tau PET has limited availability and involves exposure to ionizing radiation, which limits its widespread use as a biomarker for AD [99]. MRI holds significant potential for AD biomarker development as it is non-invasive and widely available. However, current MRI segmentation software renders out volumes for the averaged hippocampal subfields instead of providing thickness profiles of the hippocampus, limiting their ability to localize atrophy patterns spatially within the hippocampus [100].

In summary, our results demonstrated that there is a robust pattern of correlation between reduced hippocampal thickness and the reliable early biomarker tau PET. We were able to demonstrate specific regions within the hippocampus where tau accumulation is maximally correlated with reduced thickness of the hippocampus. We utilized a recently developed automated segmentation software, HippUnfold, to generate hippocampal thickness maps in a cohort of healthy elderly, patients with MCI, and subjects with AD [86]. We then used a second recently published open-source tool, BrainStat, in order to map correlations between thickness and tau PET values spatially throughout the hippocampus.

In our analysis we found both significant clusters and significant peaks, which were typically colocalized within the same region of the hippocampus. This finding enhances our confidence in the statistical significance validity of our findings. This observation suggests that thickness and tau PET values are not only highly correlated in specific locations (as measured with peaks), but that these also spatially distributed and widespread (as measured with clusters).

Interestingly, our analyses of all three areas of tau PET quantification demonstrated similar correlation patterns with reduced hippocampal thickness measurements. We found specific regions throughout the hippocampus where reduced hippocampal thickness measurements were strongly correlated with increased tau PET SUVRs. Specifically, the majority of significant clusters and peaks in the left hemisphere when correlated to the SUVRs of all three brain regions were in the body and the tail of the subiculum and CA1 regions. In the left hemisphere, there were also significant clusters and peaks in the lower end of the body of the CA3 and CA4 regions. This suggests that these regions not only have large broad correlations but also certain areas within these clusters have a more localized correlation determined by the peaks.

While significant clusters were seen in the head of the CA3 and CA4 regions when correlated to the SUVR of the entorhinal region and the inferior temporal lobe regions, there were no corresponding significant peaks in these significant clusters when running linear regression models. Due to there being only significant clusters in the head of the CA3 and CA4 subfields in the left hippocampus, this shows us that increased SUVR values in the entorhinal and inferior temporal region is correlated to large spatially contiguous regions in these subfields rather than being strongly correlated at local foci. Since there are no significant peaks in the clusters, this suggests that there is a spatially distributed pattern of correlation in that region without any highly localized vertices exhibiting a significantly stronger correlation compared to its surrounding.

Furthermore, significant clusters and peaks in the head of the CA4 and CA3 regions were not seen when linear regression was performed with the METAROI as the contrast vector. This implies that this correlation of reduced thickness in the head region of the CA3 and CA4 subfields of the left hippocampus is not seen in all of the regions affected by the tau burden of AD. This could also indicate that looking at averaged tau burden (METAROI) does not give as sensitive and specific correlations versus looking at tau burden in specific locations (entorhinal and inferior temporal). In the right hemisphere, it can be seen that the majority of significant clusters and peaks are in the body of the subiculum and the CA1 subfields as well as the head of the subiculum, CA1, CA2, and CA3 regions for all three SUVR regions evaluated. A small number of significant peaks and clusters were also seen in a small segment of the body in the

CA3 subfield. Using the SUVR value for the right inferior temporal region, we found significant clusters in the body of the CA3 similar to when the SUVR values of the METAROI and the Entorhinal region were used, but no significant peaks while the other two regions did. This shows us that increased tau burden in the right inferior temporal region is correlated to a broader area in the CA3 body where the correlation is more evenly spread in this area without specific vertices or subregions standing out as having a stronger effect.

In this study, we demonstrate the regional distribution of hippocampal subfield atrophy as correlated with tau pathology in a cohort of healthy elderly, MCI, and AD. Our data documents that reduced hippocampal thickness appears to affect specific hippocampal subfields at discrete positions along the hippocampal long axis. The other useful information is that we see both significant clusters and peaks throughout different regions of the hippocampus that are heavily involved in tau pathology, again increasing confidence that these certain regions are most atrophic with tau pathology. Our results suggest that MRI post-processing methods may hold promise to expand the use of MRI as an early biomarker for AD – given the strong correlations in our study with tau PET measurements (which are considered a relatively early marker of AD disease progression) [37].

Previous studies have shown that the subiculum and the CA1 subfields are most prominently affected in AD in the early stages of the disease and are mostly affected by neurofibrillary tangles [101]. These subfields also show the most loss of volume and thinning with increased tau burden which we were able to show in our study [102,103] . Our results are consistent with these previous findings as the majority of significant clusters were located in the subiculum and CA1. In addition, our data demonstrate the spatial and localized distribution of decreased thickness measurements throughout the hippocampal long axis. Studies have often found sparing of the CA2, CA3, and CA4 subfield regions of the hippocampus with most of the atrophy demonstrated in the subiculum region of the hippocampal body. In our analyses, a portion of the head, mainly in the CA2-CA4 of the right hemisphere, demonstrated strong correlations between reduced hippocampal thickness and AD tau pathology.

Thus, our study adds to the existing literature on hippocampal subfield segmentation in AD. While hippocampal subfields have been extensively examined in patients with AD, many previous studies have been restricted to the hippocampal body due to the difficulty of segmenting

the head and tail with in vivo MRI [86,104]. While existing automated segmentation software's have been developed which employs an atlas-based segmentation approach, previous methods have not been developed that account for the significant variability of size, shape, and folding patterns seen across human hippocampi. Finally, the majority of these studies have examined whole averaged subfield volumes when assessing atrophy, whereas methods to demonstrate atrophy patterns along the hippocampal long axis have not previously been available. HippUnfold, a recently developed open-source software, overcomes some of the limitations of previous automated segmentation approaches - as subfield atrophy can be mapped in the same space across subjects by measuring hippocampal thickness.

4.2 Future Directions

HippUnfold can be used for new emerging biomarkers such as plasma biomarkers that have shown promise in AD research, to get a better understanding of how localized atrophy of the hippocampus correlates to other existing biomarkers [105,106]. Future studies can use this technique to see how localized atrophy patterns are seen in patients who convert from MCI to AD and compare them to patients who have MCI and do not convert. This can give us more insight into how MCI patients who converted to AD differ from those who do not convert to AD. Furthermore, the analyses presented holds potential value for clinical application but require further studies demonstrating the predictive value of this method in individual patients, in contrast to the group-level analyses presented here.

4.3 Limitations

Some limitations of this study include that there were multiple patients from the AD group that were excluded from this study due to HippUnfold failing to segment the hippocampus given the extent of hippocampal atrophy. Future studies could potentially utilize T2 and T1 weighted images from AD patients for additional U-net training in order to improve applicability of HippUnfold in patients with hippocampal pathology. Another limitation is the requirements that T2 weighted 3T images require. Furthermore, as discussed above, our analysis does not provide predictive results at the individual patient level due to the group-level nature of the study design. Finally, this study had a limited scope of analysis as we examined only correlations between tau

PET and hippocampal thickness. Further analyses of HippUnfold metrics with cognitive function and existing biomarkers was beyond the scope of this project.

Chapter 5. Conclusions

AD is a growing and prominent concern around the globe. Finding biomarkers that are not only non-invasive but are also readily available is an attractive avenue for research. Finding novel ways to use MR images as an early biomarker by correlating them to tau PET is very promising. This study aims to use a novel way to analyze MR images using HippUnfold. Thickness values were acquired for all of the hippocampal subfields throughout the entire anterior-posterior axis of the hippocampus. These thickness values were then correlated to tau PET (an early reliable AD biomarker) in certain brain regions that are known to be greatly affected by tau pathology in AD. From this study, we were able to find significant clusters of reduced thickness throughout the hippocampus. This gives insights into how the tau pathology in AD affects the entire hippocampus and shows the potential of using these novel techniques as an earlier biomarker for AD. In summary our study provides important insights into the spatial distribution of atrophy in AD and can act as the basis for further studies aimed at developing novel MRI biomarkers for AD.

References

1. Love S. Neuropathological investigation of dementia: a guide for neurologists. *J Neurol Neurosurg Psychiatry*. 2005;76(suppl_5):v8-v14. doi:10.1136/jnnp.2005.080754

2. Alzheimer Society of Canada. Report summary Prevalence and monetary costs of dementia in Canada (2016): a report by the Alzheimer Society of Canada. *Health Promot Chronic Dis Prev Can Res Policy Pract*. 2016;36(10):231-232.

3. Wimo A, Seeher K, Cataldi R, et al. The worldwide costs of dementia in 2019. *Alzheimers Dement*. Published online January 8, 2023:alz.12901. doi:10.1002/alz.12901

4. Gustavsson A, Norton N, Fast T, et al. Global estimates on the number of persons across the Alzheimer's disease continuum. *Alzheimers Dement*. 2023;19(2):658-670. doi:10.1002/alz.12694

5. Joe E, Ringman JM. Cognitive symptoms of Alzheimer's disease: clinical management and prevention. *BMJ*. Published online December 6, 2019:l6217. doi:10.1136/bmj.l6217

6. Bruen PD, McGeown WJ, Shanks MF, Venneri A. Neuroanatomical correlates of neuropsychiatric symptoms in Alzheimer's disease. *Brain*. 2008;131(9):2455-2463. doi:10.1093/brain/awn151

7. Lech RK, Suchan B. The medial temporal lobe: Memory and beyond. *Behav Brain Res*. 2013;254:45-49. doi:10.1016/j.bbr.2013.06.009

8. Rogers SL, Friedman RB. The underlying mechanisms of semantic memory loss in Alzheimer's disease and semantic dementia. *Neuropsychologia*. 2008;46(1):12-21. doi:10.1016/j.neuropsychologia.2007.08.010

9. Crowell TA, Luis CA, Vanderploeg RD, Schinka JA, Mullan M. Memory Patterns and Executive Functioning in Mild Cognitive Impairment and Alzheimer's Disease. *Aging Neuropsychol Cogn*. 2002;9(4):288-297. doi:10.1076/anec.9.4.288.8772

10. Baudic S, Barba G, Thibaudet M, Smagghe A, Remy P, Traykov L. Executive function deficits in early Alzheimer's disease and their relations with episodic memory. *Arch Clin Neuropsychol*. 2006;21(1):15-21. doi:10.1016/j.acn.2005.07.002

11. Wolk D, Dickerson B. Clinical features and diagnosis of Alzheimer disease. *UpToDate*. Published online October 8, 2016. https://www.uptodate.com/contents/clinical-features-and-diagnosis-of-alzheimer-disease

12. Gorno-Tempini ML, Hillis AE, Weintraub S, et al. Classification of primary progressive aphasia and its variants. *Neurology*. 2011;76(11):1006-1014. doi:10.1212/WNL.0b013e31821103e6

13. Grossman M. Primary progressive aphasia: clinicopathological correlations. *Nat Rev Neurol*. 2010;6(2):88-97. doi:10.1038/nrneurol.2009.216

14. Brookmeyer R, Corrada MM, Curriero FC, Kawas C. Survival Following a Diagnosis of Alzheimer Disease. *Arch Neurol*. 2002;59(11):1764. doi:10.1001/archneur.59.11.1764

15. Larson EB, Shadlen MF, Wang L, et al. Survival after Initial Diagnosis of Alzheimer Disease. *Ann Intern Med*. 2004;140(7):501. doi:10.7326/0003-4819-140-7-200404060-00008

16. Markwick A, Zamboni G, De Jager CA. Profiles of cognitive subtest impairment in the Montreal Cognitive Assessment (MoCA) in a research cohort with normal Mini-Mental State Examination (MMSE) scores. *J Clin Exp Neuropsychol*. 2012;34(7):750-757. doi:10.1080/13803395.2012.672966

17. *Cognitive Screening Instruments*. Springer Berlin Heidelberg; 2016.

18. Cummings J. Alzheimer's disease diagnostic criteria: practical applications. *Alzheimers Res Ther*. 2012;4(4):35. doi:10.1186/alzrt138

19. Reisberg B, Ferris SH, Kluger A, Franssen E, Wegiel J, De Leon MJ. Mild cognitive impairment (MCI): a historical perspective. *Int Psychogeriatr*. 2008;20(1):18-31. doi:10.1017/S1041610207006394

20. Chen Y, Qian X, Zhang Y, et al. Prediction Models for Conversion From Mild Cognitive Impairment to Alzheimer's Disease: A Systematic Review and Meta-Analysis. *Front Aging Neurosci*. 2022;14:840386. doi:10.3389/fnagi.2022.840386

21. Campbell NL, Unverzagt F, LaMantia MA, Khan BA, Boustani MA. Risk Factors for the Progression of Mild Cognitive Impairment to Dementia. *Clin Geriatr Med*. 2013;29(4):873-893. doi:10.1016/j.cger.2013.07.009

22. Perl DP. Neuropathology of Alzheimer's disease. *Mt Sinai J Med N Y*. 2010;77(1):32-42. doi:10.1002/msj.20157

23. Ondrejcak T, Klyubin I, Hu NW, Barry AE, Cullen WK, Rowan MJ. Alzheimer's Disease Amyloid β-Protein and Synaptic Function. *NeuroMolecular Med*. 2010;12(1):13-26. doi:10.1007/s12017-009-8091-0

24. Hampel H, Hardy J, Blennow K, et al. The Amyloid-β Pathway in Alzheimer's Disease. *Mol Psychiatry*. 2021;26(10):5481-5503. doi:10.1038/s41380-021-01249-0

25. Paula VDJRD, Guimarães FM, Diniz BS, Forlenza OV. Neurobiological pathways to Alzheimer's disease: Amyloid-beta, TAU protein or both? *Dement Neuropsychol*. 2009;3(3):188-194. doi:10.1590/S1980-57642009DN30300003

26. Zhang X, Li Y, Xu H, Zhang Y wu. The Î[3]-secretase complex: from structure to function. *Front Cell Neurosci*. 2014;8. doi:10.3389/fncel.2014.00427

27. Bitan G, Kirkitadze MD, Lomakin A, Vollers SS, Benedek GB, Teplow DB. Amyloid β-protein (Aβ) assembly: Aβ40 and Aβ42 oligomerize through distinct pathways. *Proc Natl Acad Sci*. 2003;100(1):330-335. doi:10.1073/pnas.222681699

28. Lanoiselée HM, Nicolas G, Wallon D, et al. APP, PSEN1, and PSEN2 mutations in early-onset Alzheimer disease: A genetic screening study of familial and sporadic cases. Miller BL, ed. *PLOS Med*. 2017;14(3):e1002270. doi:10.1371/journal.pmed.1002270

29. Bekris LM, Yu CE, Bird TD, Tsuang DW. Genetics of Alzheimer disease. *J Geriatr Psychiatry Neurol*. 2010;23(4):213-227. doi:10.1177/0891988710383571

30. Moscoso A, Wren MC, Lashley T, et al. Imaging tau pathology in Alzheimer's disease with positron emission tomography: lessons learned from imaging-neuropathology validation studies. *Mol Neurodegener*. 2022;17(1):39. doi:10.1186/s13024-022-00543-x

31. Kuret J, Chirita CN, Congdon EE, et al. Pathways of tau fibrillization. *Biochim Biophys Acta BBA - Mol Basis Dis*. 2005;1739(2-3):167-178. doi:10.1016/j.bbadis.2004.06.016

32. Trejo-Lopez JA, Yachnis AT, Prokop S. Neuropathology of Alzheimer's Disease. *Neurotherapeutics*. 2022;19(1):173-185. doi:10.1007/s13311-021-01146-y

33. Richter RW, Richter BZ, eds. *Alzheimer's Disease: A Physician's Guide to Practical Management*. Springer Science+Business Media; 2004.

34. Takeda S. Progression of Alzheimer's disease, tau propagation, and its modifiable risk factors. *Neurosci Res*. 2019;141:36-42. doi:10.1016/j.neures.2018.08.005

35. Roalf DR, Moberg PJ, Xie SX, Wolk DA, Moelter ST, Arnold SE. Comparative accuracies of two common screening instruments for classification of Alzheimer's disease, mild cognitive impairment, and healthy aging. *Alzheimers Dement*. 2013;9(5):529-537. doi:10.1016/j.jalz.2012.10.001

36. Sabbagh MN, Lue LF, Fayard D, Shi J. Increasing Precision of Clinical Diagnosis of Alzheimer's Disease Using a Combined Algorithm Incorporating Clinical and Novel Biomarker Data. *Neurol Ther*. 2017;6(Suppl 1):83-95. doi:10.1007/s40120-017-0069-5

37. Jack CR, Bennett DA, Blennow K, et al. NIA-AA Research Framework: Toward a biological definition of Alzheimer's disease. *Alzheimers Dement*. 2018;14(4):535-562. doi:10.1016/j.jalz.2018.02.018

38. Gomperts SN. Lewy Body Dementias: Dementia With Lewy Bodies and Parkinson Disease Dementia. *Contin Minneap Minn*. 2016;22(2 Dementia):435-463. doi:10.1212/CON.0000000000000309

39. Jellinger KA. Dementia with Lewy bodies and Parkinson's disease-dementia: current concepts and controversies. *J Neural Transm*. 2018;125(4):615-650. doi:10.1007/s00702-017-1821-9

40. Blennow K, Zetterberg H. Biomarkers for Alzheimer's disease: current status and prospects for the future. *J Intern Med*. 2018;284(6):643-663. doi:10.1111/joim.12816

41. Sharma N. Exploring Biomarkers for Alzheimer's Disease. *J Clin Diagn Res*. Published online 2016. doi:10.7860/JCDR/2016/18828.8166

42. Strimbu K, Tavel JA. What are biomarkers? *Curr Opin HIV AIDS*. 2010;5(6):463-466. doi:10.1097/COH.0b013e32833ed177

43. Mayeux R. Biomarkers: Potential uses and limitations. *NeuroRX*. 2004;1(2):182-188. doi:10.1602/neurorx.1.2.182

44. Holland RL. What makes a good biomarker? *Adv Precis Med*. 2016;1(1):66. doi:10.18063/APM.2016.01.007

45. Chew S, Atassi N. Positron Emission Tomography Molecular Imaging Biomarkers for Amyotrophic Lateral Sclerosis. *Front Neurol*. 2019;10:135. doi:10.3389/fneur.2019.00135

46. Vogel JW, Mattsson N, Iturria-Medina Y, et al. Data-driven approaches for tau-PET imaging biomarkers in Alzheimer's disease. *Hum Brain Mapp*. 2019;40(2):638-651. doi:10.1002/hbm.24401

47. Marcus C, Mena E, Subramaniam RM. Brain PET in the diagnosis of Alzheimer's disease. *Clin Nucl Med*. 2014;39(10):e413-422; quiz e423-426. doi:10.1097/RLU.0000000000000547

48. Pooler AM, Polydoro M, Wegmann S, Nicholls SB, Spires-Jones TL, Hyman BT. Propagation of tau pathology in Alzheimer's disease: identification of novel therapeutic targets. *Alzheimers Res Ther*. 2013;5(5):49. doi:10.1186/alzrt214

49. Florean I, Penolazzi B, Menichelli A, et al. Using the ATN system as a guide for the neuropsychological assessment of Alzheimer's disease. *J Clin Exp Neuropsychol*. 2021;43(9):926-943. doi:10.1080/13803395.2022.2036327

50. Allegri RF, Chrem Méndez P, Calandri I, et al. Prognostic value of ATN Alzheimer biomarkers: 60-month follow-up results from the Argentine Alzheimer's Disease Neuroimaging Initiative. *Alzheimers Dement Diagn Assess Dis Monit*. 2020;12(1). doi:10.1002/dad2.12026

51. Ossenkoppele R, Rabinovici GD, Smith R, et al. Discriminative Accuracy of [^{18} F]flortaucipir Positron Emission Tomography for Alzheimer Disease vs Other Neurodegenerative Disorders. *JAMA*. 2018;320(11):1151. doi:10.1001/jama.2018.12917

52. Bucci M, Chiotis K, Nordberg A, for the Alzheimer's Disease Neuroimaging Initiative. Alzheimer's disease profiled by fluid and imaging markers: tau PET best predicts cognitive decline. *Mol Psychiatry*. 2021;26(10):5888-5898. doi:10.1038/s41380-021-01263-2

53. Arakawa Y, Nai Y, Shidahara M, et al. Prediction of the Clinical SUV Ratio in Amyloid PET Imaging Using a Biomathematic Modeling Approach Toward the Efficient Development of a Radioligand. *J Nucl Med*. 2017;58(8):1285-1292. doi:10.2967/jnumed.116.183566

54. Chiao P, Bedell BJ, Avants B, et al. Impact of Reference and Target Region Selection on Amyloid PET SUV Ratios in the Phase 1b PRIME Study of Aducanumab. *J Nucl Med*. 2019;60(1):100-106. doi:10.2967/jnumed.118.209130

55. Betthauser TJ. AD molecular: Imaging tau aggregates with positron emissions tomography. In: *Progress in Molecular Biology and Translational Science*. Vol 165. Elsevier; 2019:107-138. doi:10.1016/bs.pmbts.2019.07.007

56. Meyer PF, Pichet Binette A, Gonneaud J, Breitner JCS, Villeneuve S, ADNI Investigators. Characterization of Alzheimer Disease Biomarker Discrepancies Using Cerebrospinal Fluid Phosphorylated Tau and AV1451 Positron Emission Tomography. *JAMA Neurol*. 2020;77(4):508. doi:10.1001/jamaneurol.2019.4749

57. Mattsson-Carlgren N, Andersson E, Janelidze S, et al. Aβ deposition is associated with increases in soluble and phosphorylated tau that precede a positive Tau PET in Alzheimer's disease. *Sci Adv*. 2020;6(16):eaaz2387. doi:10.1126/sciadv.aaz2387

58. Biel D, Brendel M, Rubinski A, et al. Tau-PET and in vivo Braak-staging as prognostic markers of future cognitive decline in cognitively normal to demented individuals. *Alzheimers Res Ther*. 2021;13(1):137. doi:10.1186/s13195-021-00880-x

59. Jack CR, Knopman DS, Jagust WJ, et al. Hypothetical model of dynamic biomarkers of the Alzheimer's pathological cascade. *Lancet Neurol*. 2010;9(1):119-128. doi:10.1016/S1474-4422(09)70299-6

60. Palmqvist S, Hertze J, Minthon L, et al. Comparison of Brief Cognitive Tests and CSF Biomarkers in Predicting Alzheimer's Disease in Mild Cognitive Impairment: Six-Year Follow-Up Study. Breitner JCS, ed. *PLoS ONE*. 2012;7(6):e38639. doi:10.1371/journal.pone.0038639

61. Khoury R, Ghossoub E. Diagnostic biomarkers of Alzheimer's disease: A state-of-the-art review. *Biomark Neuropsychiatry*. 2019;1:100005. doi:10.1016/j.bionps.2019.100005

62. Berger A. Magnetic resonance imaging. *BMJ*. 2002;324(7328):35. doi:10.1136/bmj.324.7328.35

63. Graeber MB, Mehraein P. Reanalysis of the first case of Alzheimer's disease. *Eur Arch Psychiatry Clin Neurosci*. 1999;249(S3):S10-S13. doi:10.1007/PL00014167

64. Mu Y, Gage FH. Adult hippocampal neurogenesis and its role in Alzheimer's disease. *Mol Neurodegener*. 2011;6(1):85. doi:10.1186/1750-1326-6-85

65. Squire LR, Genzel L, Wixted JT, Morris RG. Memory Consolidation. *Cold Spring Harb Perspect Biol*. 2015;7(8):a021766. doi:10.1101/cshperspect.a021766

66. Jin ZY. Advances in MRI-based biomarkers of Alzheimer's disease. In: ; 2020:020017. doi:10.1063/5.0020494

67. Van Oostveen WM, De Lange ECM. Imaging Techniques in Alzheimer's Disease: A Review of Applications in Early Diagnosis and Longitudinal Monitoring. *Int J Mol Sci*. 2021;22(4):2110. doi:10.3390/ijms22042110

68. Jack CR, Knopman DS, Jagust WJ, et al. Tracking pathophysiological processes in Alzheimer's disease: an updated hypothetical model of dynamic biomarkers. *Lancet Neurol*. 2013;12(2):207-216. doi:10.1016/S1474-4422(12)70291-0

69. Vos De Wael R, Larivière S, Caldairou B, et al. Anatomical and microstructural determinants of hippocampal subfield functional connectome embedding. *Proc Natl Acad Sci*. 2018;115(40):10154-10159. doi:10.1073/pnas.1803667115

70. DeKraker J, Köhler S, Khan AR. Surface-based hippocampal subfield segmentation. *Trends Neurosci*. 2021;44(11):856-863. doi:10.1016/j.tins.2021.06.005

71. Broadhouse KM, Mowszowski L, Duffy S, et al. Memory Performance Correlates of Hippocampal Subfield Volume in Mild Cognitive Impairment Subtype. *Front Behav Neurosci*. 2019;13:259. doi:10.3389/fnbeh.2019.00259

72. Apostolova LG, Dinov ID, Dutton RA, et al. 3D comparison of hippocampal atrophy in amnestic mild cognitive impairment and Alzheimer's disease. *Brain*. 2006;129(11):2867-2873. doi:10.1093/brain/awl274

73. Apostolova LG, Dutton RA, Dinov ID, et al. Conversion of Mild Cognitive Impairment to Alzheimer Disease Predicted by Hippocampal Atrophy Maps. *Arch Neurol*. 2006;63(5):693. doi:10.1001/archneur.63.5.693

74. Frisoni GB, Ganzola R, Canu E, et al. Mapping local hippocampal changes in Alzheimer's disease and normal ageing with MRI at 3 Tesla. *Brain*. 2008;131(12):3266-3276. doi:10.1093/brain/awn280

75. Chételat G, Fouquet M, Kalpouzos G, et al. Three-dimensional surface mapping of hippocampal atrophy progression from MCI to AD and over normal aging as assessed using voxel-based morphometry. *Neuropsychologia*. 2008;46(6):1721-1731. doi:10.1016/j.neuropsychologia.2007.11.037

76. Whitwell JL, Przybelski SA, Weigand SD, et al. 3D maps from multiple MRI illustrate changing atrophy patterns as subjects progress from mild cognitive impairment to Alzheimer's disease. *Brain*. 2007;130(7):1777-1786. doi:10.1093/brain/awm112

77. Crum WR, Scahill RI, Fox NC. Automated Hippocampal Segmentation by Regional Fluid Registration of Serial MRI: Validation and Application in Alzheimer's Disease. *NeuroImage*. 2001;13(5):847-855. doi:10.1006/nimg.2001.0744

78. Helaly HA, Badawy M, Haikal AY. Toward deep MRI segmentation for Alzheimer's disease detection. *Neural Comput Appl*. 2022;34(2):1047-1063. doi:10.1007/s00521-021-06430-8

79. Hamwood J, Schmutz B, Collins MJ, Allenby MC, Alonso-Caneiro D. A deep learning method for automatic segmentation of the bony orbit in MRI and CT images. *Sci Rep*. 2021;11(1):13693. doi:10.1038/s41598-021-93227-3

80. Boccardi M, Ganzola R, Bocchetta M, et al. Survey of protocols for the manual segmentation of the hippocampus: preparatory steps towards a joint EADC-ADNI harmonized protocol. *J Alzheimers Dis JAD*. 2011;26 Suppl 3(0 3):61-75. doi:10.3233/JAD-2011-0004

81. Yamanakkanavar N, Choi JY, Lee B. MRI Segmentation and Classification of Human Brain Using Deep Learning for Diagnosis of Alzheimer's Disease: A Survey. *Sensors*. 2020;20(11):3243. doi:10.3390/s20113243

82. Srinivasan D, Erus G, Doshi J, et al. A comparison of Freesurfer and multi-atlas MUSE for brain anatomy segmentation: Findings about size and age bias, and inter-scanner stability in multi-site aging studies. *NeuroImage*. 2020;223:117248. doi:10.1016/j.neuroimage.2020.117248

83. Yushkevich PA, Pluta JB, Wang H, et al. Automated volumetry and regional thickness analysis of hippocampal subfields and medial temporal cortical structures in mild cognitive impairment: Automatic Morphometry of MTL Subfields in MCI. *Hum Brain Mapp*. 2015;36(1):258-287. doi:10.1002/hbm.22627

84. Zeidman P, Maguire EA. Anterior hippocampus: the anatomy of perception, imagination and episodic memory. *Nat Rev Neurosci*. 2016;17(3):173-182. doi:10.1038/nrn.2015.24

85. Haast RAM, Lau JC, Ivanov D, Menon RS, Uludağ K, Khan AR. Effects of MP2RAGE B1+ sensitivity on inter-site T1 reproducibility and hippocampal morphometry at 7T. *NeuroImage*. 2021;224:117373. doi:10.1016/j.neuroimage.2020.117373

86. DeKraker J, Haast RA, Yousif MD, et al. Automated hippocampal unfolding for morphometry and subfield segmentation with HippUnfold. *eLife*. 2022;11:e77945. doi:10.7554/eLife.77945

87. De Wael RV, Bayrak Ş, Benkarim O, et al. *BrainStat: A Toolbox for Brain-Wide Statistics and Multimodal Feature Associations*. Neuroscience; 2022. doi:10.1101/2022.01.18.476795

88. Weber CJ, Carrillo MC, Jagust W, et al. The Worldwide Alzheimer's Disease Neuroimaging Initiative: ADNI-3 updates and global perspectives. *Alzheimers Dement N Y N*. 2021;7(1):e12226. doi:10.1002/trc2.12226

89. Alzheimer's Disease Neuro Imaging III (ADNI3) MRI Analysis User Document. Published online June 28, 2018.

90. Chen Y, Almarzouqi SJ, Morgan ML, Lee AG. T2-Weighted Image. In: Schmidt-Erfurth U, Kohnen T, eds. *Encyclopedia of Ophthalmology*. Springer Berlin Heidelberg; 2018:1750-1752. doi:10.1007/978-3-540-69000-9_1229

91. Gorgolewski KJ, Alfaro-Almagro F, Auer T, et al. BIDS apps: Improving ease of use, accessibility, and reproducibility of neuroimaging data analysis methods. Schneidman D, ed. *PLOS Comput Biol*. 2017;13(3):e1005209. doi:10.1371/journal.pcbi.1005209

92. Filobello-Nino U, Vazquez-Leal H, Herrera-May A, et al. The study of heat transfer phenomena by using modified homotopy perturbation method coupled by Laplace transform. *Therm Sci*. 2020;24(2 Part B):1105-1115. doi:10.2298/TSCI180108204F

93. Charpentier CJ, Faulkner P, Pool ER, et al. How representative are neuroimaging samples? Large-scale evidence for trait anxiety differences between fMRI and behaviour-only research participants. *Soc Cogn Affect Neurosci*. 2021;16(10):1057-1070. doi:10.1093/scan/nsab057

94. Dettori JR, Norvell DC, Chapman JR. Fixed-Effect vs Random-Effects Models for Meta-Analysis: 3 Points to Consider. *Glob Spine J*. 2022;12(7):1624-1626. doi:10.1177/21925682221110527

95. Wooditch A, Johnson NJ, Solymosi R, Medina Ariza J, Langton S. Correction to: A Beginner's Guide to Statistics for Criminology and Criminal Justice Using R. In: *A Beginner's Guide to Statistics for Criminology and Criminal Justice Using R*. Springer International Publishing; 2021:C1-C1. doi:10.1007/978-3-030-50625-4_16

96. de Winter JCF. Using the Student's t-test with extremely small sample sizes. doi:10.7275/E4R6-DJ05

97. Nichols TE. Multiple testing corrections, nonparametric methods, and random field theory. *NeuroImage*. 2012;62(2):811-815. doi:10.1016/j.neuroimage.2012.04.014

98. Humpel C. Identifying and validating biomarkers for Alzheimer's disease. *Trends Biotechnol*. 2011;29(1):26-32. doi:10.1016/j.tibtech.2010.09.007

99. Rowley PA, Samsonov AA, Betthauser TJ, Pirasteh A, Johnson SC, Eisenmenger LB. Amyloid and Tau PET Imaging of Alzheimer Disease and Other Neurodegenerative Conditions. *Semin Ultrasound CT MRI*. 2020;41(6):572-583. doi:10.1053/j.sult.2020.08.011

100. Xie L, Wisse LEM, Pluta J, et al. Automated segmentation of medial temporal lobe subregions on in vivo T1-weighted MRI in early stages of Alzheimer's disease. *Hum Brain Mapp*. 2019;40(12):3431-3451. doi:10.1002/hbm.24607

101. Mueller SG, Chao LL, Berman B, Weiner MW. Evidence for functional specialization of hippocampal subfields detected by MR subfield volumetry on high resolution images at 4 T. *NeuroImage*. 2011;56(3):851-857. doi:10.1016/j.neuroimage.2011.03.028

102. Hoesen GWV, Hyman BT. Chapter 32 Hippocampal formation: anatomy and the patterns of pathology in Alzheimer's disease. In: *Progress in Brain Research*. Vol 83. Elsevier; 1990:445-457. doi:10.1016/S0079-6123(08)61268-6

103. Wisse LEM, Biessels GJ, Heringa SM, et al. Hippocampal subfield volumes at 7T in early Alzheimer's disease and normal aging. *Neurobiol Aging*. 2014;35(9):2039-2045. doi:10.1016/j.neurobiolaging.2014.02.021

104. Mueller SG, Stables L, Du AT, et al. Measurement of hippocampal subfields and age-related changes with high resolution MRI at 4T. *Neurobiol Aging*. 2007;28(5):719-726. doi:10.1016/j.neurobiolaging.2006.03.007

105. Moscoso A, Grothe MJ, Ashton NJ, et al. Time course of phosphorylated-tau181 in blood across the Alzheimer's disease spectrum. *Brain*. 2021;144(1):325-339. doi:10.1093/brain/awaa399

106. Moscoso A, Grothe MJ, Ashton NJ, et al. Longitudinal Associations of Blood Phosphorylated Tau181 and Neurofilament Light Chain With Neurodegeneration in Alzheimer Disease. *JAMA Neurol*. 2021;78(4):396. doi:10.1001/jamaneurol.2020.4986